NUMERICAL SIMULATION OF THE CASTING PROCESS

by

H C Bowles

A thesis submitted in partial fulfillment of the requirements for the degree of Master of Science in Engineering

Department of Mechanical Engineering

University of Cape Town

October 1989

DECLARATION

This is to certify that the results, calculations and other work presented in this thesis are essentially my own work, and that no part of it has been submitted for a degree at any other university.

Signed by candidate

H C Bowles

October 1989

ACKNOWLEDGEMENTS

I acknowledge, and greatly appreciate, the help of the following people:

Professor J B Martin and Dr C D Mercer, under whose joint supervision this thesis was conducted.

CSIR's Division of Materials Science and Technology for support and collaboration.

Robert McAdie for help and guidance.

Fellow colleagues at the Centre of Research in Computational and Applied Mechanics for their willing assistance.

The Foundation for Research and Development (FRD) for their financial assistance.

ABSTRACT

The increasingly competitive market for cast products has required the development of higher quality and lower cost products. Although conventional process development techniques have improved, the cost and time associated to process development needs to be reduced. A faster and more cost effective development method is required. Numerical modelling techniques provide a means by which casting design and process parameters can be optimized with minimum use of prototypes.

This thesis reviews the current state of the art in solidification modelling. A typical casting problem is modelled and the numerical results compared against measured temperatures. From this investigation it is concluded that further work is required to obtain, and accurately model the material properties and complex radiation behaviour within the fibrous insulation.

Table of Contents

Declaration i

Dedication ii

Acknowledgements iii

Abstract iv

Table of Contents v

Nomenclature vii

1. Introduction 1

2. The Solidification Process 3
   - 2.1 Foundry Practice 3
   - 2.2 Solidification Mechanics 5
     - 2.2.1 Microstructures in Castings 6
     - 2.2.3 Heat and Mass Transfer During Solidification 9
       - 2.2.2.1 Thermal Conduction 10
       - 2.2.2.2 Thermal Convection and Fluid Flow 10
       - 2.2.2.3 Metal-Mould Interface Heat Transfer 12
       - 2.2.2.4 Thermal Boundary Conditions 14
   - 2.3 Problems Associated to the Casting Process 17
     - 2.3.1 Voids and Hot Tears 18
     - 2.3.2 Porosity 18
     - 2.3.3 Segregation 19

3. Overview of Numerical Modelling of Solidification 22
   - 3.1 Analytical Methods 22
   - 3.2 Numerical Methods 25
     - 3.2.1 Finite Difference Method 27
     - 3.2.2 Finite Element Method 30

4. Numerical Investigation of Casting Example 34
   - 4.1 Experimental Castings 35
     - 4.1.1 Instrumented Mould Layout 35
     - 4.1.2 Experimental Procedure 36
     - 4.1.3 Observations 37
   - 4.2 Numerical Model 39

4.2.1 ABAQUS Finite Element Code 40
4.2.2 Finite Element Mesh 41
4.2.2.1 Mesh Sensitivity Study 42
4.2.3 Material Property and Boundary Conditions 44
4.2.3.1 Parametric Study 44
4.2.3.2 One-Dimensional Study 49
4.2.4 Comparison of Numerical and Experimental Results 50
4.2.5 Discussion of Differences 61
4.2.5.1 Uncertainty of Material Properties 62
4.2.5.2 Uncertainty of Boundary conditions 62
4.2.5.3 Experimental Error 63
4.2.5.4 Numerical Model Limitations 65

5. Summary and Conclusions 67
5.1 Summary 67
5.2 Conclusions 68
5.3 Future Work 69

References 72

Appendix A 76
Appendix B 81
Appendix C 85
Appendix D 87
Appendix E 90

NOMENCLATURE

This is a list of the various symbols used in the main text of this thesis.

Symbols

A	area
C	specific heat capacity
F	radiation view factor
Fo	Fourier number
G	thermal gradient
Gr	Grashof number
H	enthalpy
K	conductivity
L	latent heat of fusion
N_l	interpolation or shape functions
P	pressure
Pr	Prandtl number
Q	internal heat generation
Ra	Rayleigh number
S	liquid-solid interface position
T	temperature
T_L	liquidus temperature
T_S	solidus temperature
$\hat{T}$	local temperature change
ΔT_m	alloy solidification temperature range
V	volume
c	speed of light
d	dendrite arm spacing
e	radiation emittance
f	volume fraction
g_r	acceleration due to gravity
h	Plancks constant
h_l	interface conductance coefficient
h_c	convection coefficient
k	equilibrium partition ratio
l	element length
ℓ	characteristic length
m	refraction index

q	heat flux
q_{La}	latent heat flux
q_{Se}	sensible heat flux
t	time
t_f	total solidification time
$\hat{t}_f$	local solidification time
Δt	time increment
v	velocity
w	test function
α	thermal diffusivity
β	volumetric coefficient of expansion
$\hat{\beta}$	solidification shrinkage parameter
β	extinction coefficient
ε	emissivity
κ	Boltzmann constant
λ	wavelength
λ^h	eigenvalue
μ	dynamic viscosity
ν	kinematic viscosity which is given by $\nu = \frac{\mu}{\rho}$
ρ	density
σ	Stefan-Boltzmann constant
$\mathcal{T}$	dendrite tortuosity
υ	frequency
$\mathbb{C}$	solute concentration
$\mathbb{C}^*$	concentration at the solid-liquid interface
$\mathbb{K}$	permeability

Subscripts	
L	liquid
S	solid
m	mushy region
p	porosity
0	initial condition

Special Symbols	
$\cdot$	vector dot product
[ ]	matrix
$\lvert\ \rvert$	absolute value
∇	gradient operator

1. INTRODUCTION

Casting is a manufacturing process dating back to early human civilizations in Mesopotamia. The process has several inherent problems that can produce defects lowering the quality and mechanical properties of the product. Standard procedures of design optimization involve the production of numerous full scale production prototypes. These prototype castings are cast using different process parameters and mould designs. Each is individually evaluated to determine the mechanical properties and extent of defects. This trial and error approach becomes very costly, and wasteful machining processes are often employed to produce complex products as the required casting development program is too expensive. There is therefore a need for cost effective prototype development methods for the casting process. This need inspired various researchers to develop numerical modelling techniques capable of simulating latent heat release and heat transfer during solidification. The two most commonly used techniques are the finite difference and finite element methods. Both evaluate temperatures at discrete points, which may be interpolated to approximate the global temperature field. These numerical techniques can be used by the foundry engineer to predict likely defects, and thereby reduce the number of prototypes required to optimize the casting process.

Modern casting processes have become increasingly specialized. The use of numerical methods has played a large role in the development of the directional and single crystal casting technology. For example, complex products which could previously only be produced by traditional machining processes are now being cast. New superalloys, capable of withstanding higher operating temperatures and stresses are being developed for the casting of gas turbine components. Current research and development is aimed at extending the existing numerical modelling technology to be able to model microstructural evolution, likelihood of defects and residual stresses and strains. The ability to model these parameters will enable engineers and foundrymen to develop and produce new castings, with superior properties and lower associated development costs.

The aim of this thesis is to review the current state of the art in solidification modelling. To achieve this objective a general finite element package is employed to investigate a typical casting problem. This numerical

investigation is used to determine the numerical model's capabilities and limitations in correctly predicting temperature profiles and defects. An understanding of the basic principles of casting, solidification mechanics and numerical modelling is required prior to performing this investigation.

This thesis begins with an introduction to the foundry practice, solidification mechanics and associated defects. This is followed by a brief discussion of analytical and numerical modelling techniques. In the following chapter an investment casting problem is numerically modelled using the finite element method. The numerically predicted temperatures are compared with experimentally measured temperatures. The correlation and possible reasons for differences are discussed. Conclusions are drawn from this discussion. The scope for future work is discussed and suggestions made.

2. The Solidification Process

2.1 Foundry Practice

The metal casting process dates back to 4000 B.C., where it was used to produce tools, weapons and religious artifacts. Since its inception the casting process has consisted of making and preparing the mould, melting and pouring the metal, and cleaning the resultant casting.

The mould may take various forms depending on the casting process being employed. In general it consists of a gating system, riser and mould cavity, as shown in figure 2.1 for two sand castings.

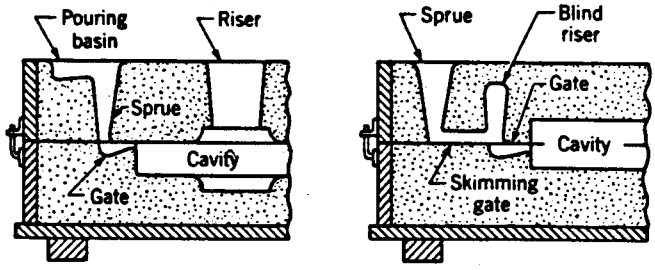

Figure 2.1 Two typical sand casting moulds.

The gating system is the passageway used for bringing liquid metal into the mould cavity. It is usually consists of a pouring basin, a vertical passage known as a sprue, and a gate through which the metal flows from the sprue base into the mould cavity. In large castings a runner may be used to distribute molten metal from the sprue base into several gate passageways around the cavity. The mould cavity has the required shape of the resultant product, though some allowances have to be made for shrinkage and distortion which may occur as the casting cools. The riser is a vertical column of metal which is not part of the actual product. Its function is to feed molten metal into the casting cavity to compensate for the solidification shrinkage, and ideally it should be the last to solidify. Solidification should proceed directionally from the mould surface towards the riser, in order to maintain a constant supply of liquid metal to compensate for shrinkage. This can be promoted by imposing a temperature gradient between the riser and the mould surface, using chills, exothermic and insulating materials. Chills, usually metallic, absorb

heat from the solidifying metal at a rapid rate. Exothermic materials react chemically giving off heat and slow down solidification. Insulating materials may also be used to reduce the moulds heat losses and slow down the rate of solidification.

Castings can be divided into two broad categories, equiaxed and directional, according to the solidification front progression. The progression in equiaxed castings is multidirectional. The overall microstructure has no preferred orientation and gives rise to isotropic mechanical properties. Directional solidification on the other hand progresses directionally and leads to directional crystal growth, and this increases the mechanical properties in the growth direction. These properties can be increased further by producing a single crystal casting. A review of directional and single crystal castings is given in Versnyder and Shank [1]. Various casting techniques are used in industry. Here, two common techniques are discussed.

In sand castings the sand is rammed into place over a pattern, providing the required impressions in the upper and lower mould halves. The mould segments are made separately and assembled to produce a mould cavity with the shape of the desired casting. The sand contains a small percentage of water, clay and sometimes binding agents to retain the shape of the impression. The pattern may be removable, e.g. wood or metal, or disposable, e.g. polystyrene, in which case it is vaporized by the liquid metal. Figure 2.1 shows the typical layout of two sand moulds. The metal is poured in the pouring basin and allowed to solidify. After the casting has cooled sufficiently it is shaken from the mould. The riser and gating systems are removed and the casting is cleaned.

Another technique is investment casting, using a ceramic shell mould produced by the lost wax method. The lost wax method uses positive wax patterns of the desired product. A number of these patterns together with wax risers etc, are assembled into a cluster arrangement. The ceramic shell mould is built up by repeatedly dipping this wax cluster into ceramic slurries and powders. The mould is then allowed to dry. The pattern is then melted out of the mould, which is then fired in order to remove all moisture and organic material. The mould is then ready for usage. An illustrated review of the lost wax casting method is given by Taylor [2]. During the investment casting process the mould is preheated and then transported to a pouring furnace, where pouring

may take place under vacuum conditions to prevent oxidation of the metal. The ceramic shell breaks away from the casting during cooling and leaves an accurate casting with a very smooth surface finish. Figure 2.2 shows a shell mould used to directionally cast turbine blades [1].

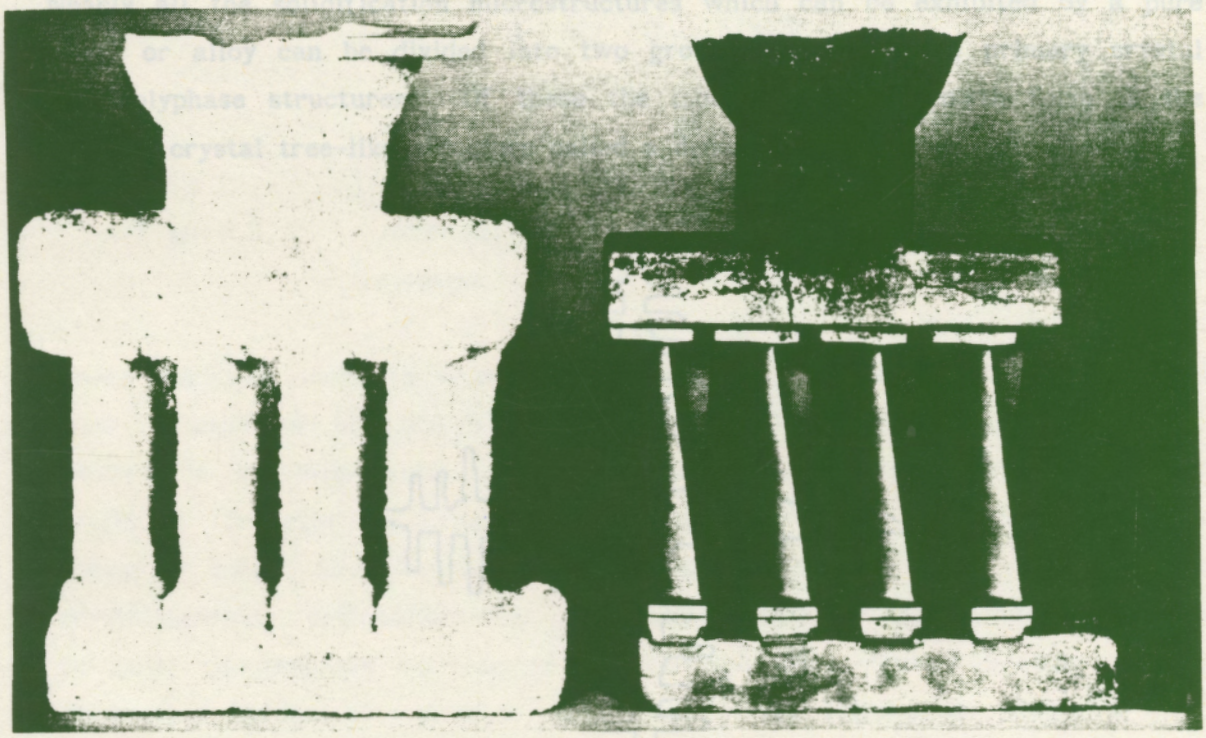

Figure 2.2 Directionally solidified gas turbine blade casting and mould.

As in all manufacturing processes, the objective is to produce a product free of defects, with the desired mechanical properties, at a competitive price.

2.2 Solidification Mechanics

During solidification the metal has to cool and dissipate the evolved latent heat of fusion. This entails a combined heat and mass transfer. The rate and manner in which this heat is transferred influences the solidification within the casting. The phase change occurring during casting transforms the liquid metal into a crystal matrix. The resultant microstructure is of great importance as it influences the products overall mechanical properties of the casting. Irregularities during solidification result in defects which reduce

these properties. A brief overview of crystal formation and the related heat and mass transfer mechanisms is given below.

2.2.1 Microstructures in Castings

Nearly all the solidification microstructures which can be exhibited by a pure metal or alloy can be divided into two groups: single phase primary crystal and polyphase structures. Of these the most important growth form is the primary crystal tree-like structure called a dendrite, depicted in figure 2.3.

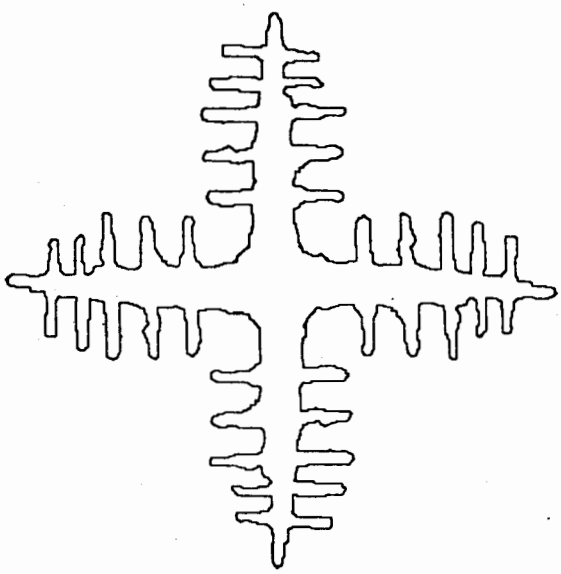

Figure 2.3 Dendrite structure as seen in metals.

The central portion of the structure is termed the primary dendrite arm, and the perpendicular rod like protrusions are called secondary dendrite arms. These dendrites are either columnar or equiaxed. The formation of a columnar dendrite begins with the breakdown of an unstable planar solid-liquid interface. Perturbations amplify and the tips grow more rapidly than the depressions. These perturbations form cells which grow parallel and opposite to the direction of heat flow. If instabilities arise between cells, side branching occurs and dendrites form, as shown in figure 2.4. [3].

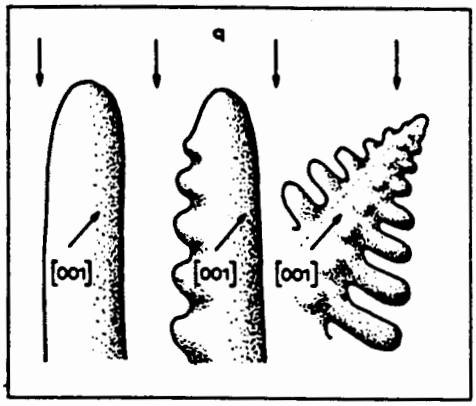

Figure 2.4 Intercellular instabilities resulting in dendrite formation.

These dendrites adopt an orientation which is as close as possible to the heat flow direction or opposite it, but follow one of the preferred growth axes, which are crystallographically determined. The driving forces leading to preferred dendrite directions are interface kinetics, anisotropic surface energy or both. Small driving forces can cause dendrites to grow out of their crystallographic orientation [4]. Equiaxed dendrites are similar to their columnar counterparts but require a nucleation site or seed crystal to form. They also differ to columnar dendrites in that there is little, if any, preferential orientation in the heat flow direction. Equiaxed dendrites grow along all the available preferred directions when heat extraction is isotropic.

Studies on transparent alloys show that columnar dendrites can adjust their primary spacing during growth. If the spacing is too close, a primary arm falls behind and is engulfed. If on the other hand the spacing is too large, a tertiary arm growing from a secondary arm catches up to the growing primary tips and becomes one of them, as shown in figure 2.5 [4].

Figure 2.5 Formation of new primary arms by branching from secondary arms.

The driving force is the constitutional supercooling in the region between the two primary arms, which is reduced by branching.

Primary and secondary arm spacings are important as they both influence the mechanical properties of the material. The primary dendrite spacing depends on the product of thermal gradient and growth rate. The secondary dendrite arm spacing depends directly on the cooling rate for a wide variety of alloys, both columnar and equiaxed. These relationships can be expressed by:

$$d = a\,\hat{t}_f^{\,n} = b(GR)^{-n} \qquad (2.1)$$

where d is the dendrite arm spacing,
$\hat{t}_f$ is the local solidification time,
GR is the growth rate,
a and b are constants,
and exponent n is in the range 1/3 to 1/2 for secondary spacings and very close to 1/2 for primary spacings.

The final secondary dendrite arm spacing observed in a fully solidified casting is usually much coarser than the initial one. Coarsening occurs when some arms become unstable during solidification and melt while others continue to grow. Three idealized models have been proposed for this coarsening behaviour [4]. As the coarsening proceeds the influence of the original spacing on the final casting diminishes, and a mechanism other than constitutional supercooling determines the final spacing.

Another effect of coarsening is to decrease microsegregation. The arms which form early on have a low solute content, and when they subsequently remelt they precipitate with a higher solute content. In this manner the

microsegregation present is reduced. Another effect is grain multiplication. The coarsening mechanism melts off various dendrite arms which are carried away by convection currents into neighbouring regions of supercooled liquid, and form new crystals. Equiaxed crystals are often formed in this manner. Reducing this fluid convection leads to columnar structures, with fewer but larger grains in total.

In a typical ingot casting there is usually three distinguishable regions, shown in figure 2.6 [3].

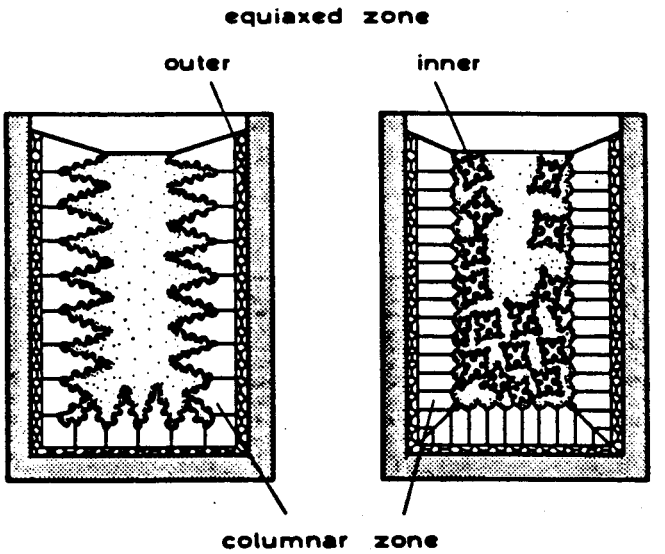

Figure 2.6 Zone formation within an ingot during solidification.

At the metal-mould interface, the cooling rate is at its highest due to the relatively low initial temperature of the mould. Many small grains, with random orientation, are nucleated at the mould surface. These grains rapidly become dendritic and develop arms which grow along all preferred crystallographic directions, and form an outer equiaxed zone. These develop into columnar grains which grow inwards towards the center of the ingot, where another equiaxed region forms, largely due to growth of detached dendrite arms in the remaining slightly undercooled liquid.

2.2.2 Heat and Mass Transfer During Solidification

As mentioned above, solidification requires both heat and mass transfer.

These are discussed below.

2.2.2.1 Thermal Conduction

The classical theory of heat conduction describes rather complicated physical processes on the macroscopic basis of the Fourier-Biot law of heat conduction. For isotropic materials this is

$$\mathbf{q} = -K \nabla T \tag{2.2}$$

Where **q** is the heat flux per unit area,
K is the thermal conductivity,
T is the temperature.

The conductivity is dependent on chemical composition, pressure and temperature, but independent of material thickness, temperature gradient or heat flux. The transient heat transfer equation is written as,

$$\nabla \cdot K \nabla T + Q = \rho C \frac{\partial T}{\partial t} \tag{2.3}$$

where ρ and C are the density and specific heat respectively,
Q is an internal heat generation term,

The first term on the right hand side represents the heat absorbed/rejected by a body during heating/cooling respectively and is called the sensible heat.

2.2.2.2 Thermal Convection and Fluid Flow

An important and sometimes neglected aspect of solidification is the convection occurring within the liquid metal. This occurs as a result of the density differences arising from temperature gradients within the liquid metal, and the momentum of pouring. The convection currents transport heat and mass within the casting cavity, and dissipates the liquid's superheat and reduces any thermal gradients present. Convection also influences the structure and sometimes composition of the solidifying metal. It plays a dominant role in the columnar-equiaxed transition. Small temperature

differences are able to produce strong convection currents. The important variables influencing the severity of thermal convection are contained in the Grashof and Prandtl numbers, where

$$Gr = \frac{g_r \ell \beta^3 \Delta T}{\nu^2} \tag{2.4}$$

and

$$Pr = \frac{C \mu}{K} \tag{2.5}$$

where g_r is acceleration of gravity,
ℓ is the characteristic length,
β is the volumetric coefficient of expansion,
ΔT is the temperature difference,
ν is the kinematic viscosity,
μ is the viscosity,
C is the specific heat of the liquid,
K is the conductivity of the liquid.

The product of these two numbers is termed the Rayleigh number, Ra, and represents the ratio of buoyancy forces to viscous forces in the liquid. The transient heat transfer equation given by equation (2.3) requires an additional term to include convection, and can be written as,

$$\nabla \cdot K \nabla T + Q = \rho C \frac{\partial T}{\partial t} + \rho C v \cdot \nabla T \tag{2.6}$$

The velocity field in the liquid metal, v, is governed by continuity and Navier-Stokes equations.

Fluid flow does not only exist in the bulk liquid, but also in the interdendritic regions. During the early stages of solidification both liquid and solid move to compensate for solidification shrinkage. As solidification progresses, a point is reached where the solid is no longer able to move readily and a solid skeleton begins to form. From this point solidification shrinkage is fed by interdendritic flow. This flow is driven by solidification shrinkage, thermal contractions and gravity. The dendrite arm spacing is usually in the range of 10 to 100 μm, and so the channels available for fluid flow are very small. This fluid flow can be approximated as that through porous media. Thus, the mean interdendritic flow velocity vis

linearly related to the pressure gradient as given by Darcy's law,

$$\mathbf{v} = - \frac{\mathbb{K}}{\mu f_L} \left(\nabla P + \rho g_r \right) \tag{2.7}$$

where $\mathbb{K}$ is permeability,
P is pressure,
g_r is acceleration due to gravity,
μ is viscosity,
f_L is liquid volume fraction.

The permeability $\mathbb{K}$ depends on geometry and pore size, and thus also on liquid fraction. The density in equation (2.7) changes as solidification progresses and is not constant. This change is governed by the conservation of mass which can be stated as,

$$\frac{\partial \bar{\rho}}{\partial t} = - \nabla \cdot \rho_L f_L \mathbf{v} \tag{2.8}$$

where t is time and $\bar{\rho}$ is the average density defined by,

$$\bar{\rho} = \rho_S f_S + \rho_L f_L \tag{2.9}$$

where ρ and f are the densities and volume fractions, of the liquid and solid respectively. These respective volume fractions change as solidification progresses. The above equations provide the basic relations for interdendritic flow during solidification.

2.2.2.3 Metal Mould Interface Heat Transfer .

During solidification, heat is transferred away from the metal out to the surrounding environment. This requires heat transfer across the metal-mould interface. This transfer is inhibited by thermal impedances due to contact resistance and gap formation. Contact resistance occurs between two surfaces which are not perfectly smooth. The interface consists of isolated points of contact with voids in between. Thermal conduction takes place at the points of contact, and heat is transferred by radiation, conduction and convection if entrapped gas is present, across the voids. The actual contact area is only a small fraction of the nominal area and this reduces the overall heat transfer

across the interface. This impedance is dependent on the applied pressure keeping the surfaces in contact. Gaps forms between the metal and mould interface as a result of thermal contraction of both the casting and mould. The size of the gap varies according to the geometry and position with respect to the casting.

The thermal contraction, solidification shrinkage, metal's plastic deformation during freezing, and oxide growth on the metal surface all contribute to the overall thermal interface impedance, which usually varies considerably with time. The impedance also depends on the geometry of the casting. A hemispherical shell casting can be used to illustrate this point. At the outer radial surface the metal-mould interface tends to shrink away from the mould surface, while at the inner interface the metal contracts onto the mould surface. Gap formation and thermal impedance characteristics are thus dependent on casting geometry.

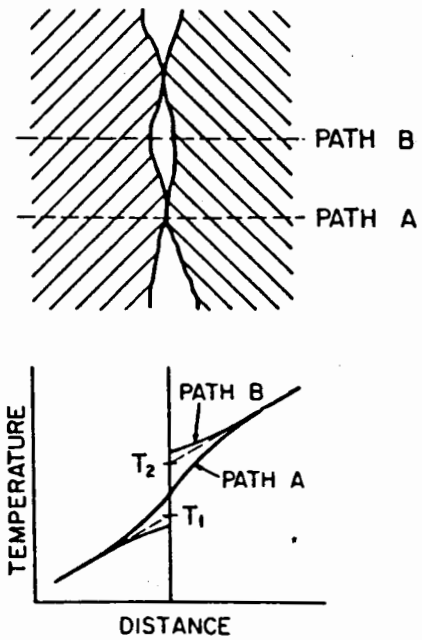

Figure 2.7 Temperature profiles across a surface interface.

Figure 2.7 shows an interface cross section and gives a typical temperature distribution across it. The mechanics of the interface heat transfer are complex. An effective thermal conductance which accounts for conductive, convective and radiative heat exchange across the gap is defined as a compromise between mathematical simplicity and physical phenomenon [5]. The

macroscopic average interfacial conductance h_i is defined by,

$$h_i = \frac{q}{T_2 - T_1} \tag{2.10}$$

where q is the average heat flux across the interface,
T_1 and T_2 are two fictitious surface temperatures based on extrapolations from interior temperatures on both sides of the interface, as depicted in figure 2.7.

2.2.2.4 Thermal Boundary Conditions

The heat absorbed by the mould is dissipated to the surrounding environment. The mode of thermal transfer may be conduction, convection or radiation. Thermal conduction between the mould and surrounding environment takes place at points of contact. This transfer is governed by the Fourier-Biot law, equation (2.2), and equation (2.10) if contact resistance is taken into account. Convection will occur in the presence of a fluid, such as air. This may be free or forced convection. Free convection occurs as a result of the natural fluid motion caused by density changes arising from thermal gradients, while forced convection is due to imposed air currents. Free convection can be illustrated by considering a hot vertical plate. The air coming in contact with it, heats up and expands. Due to gravity this heated air, with lower density, rises and transports heat away. As in the case of convection in liquid metal, the Grashof and Prandtl numbers, equations (2.4) and (2.5), give a measure of the convection. The macroscopic convection heat transfer can be defined by the Neumann equation,

$$q = h_c (T_W - T_\infty) \tag{2.11}$$

where q is the heat transfer per unit surface area,
T_W is the surface temperature,
T_∞ is the ambient fluid temperature,
h_c is the convection heat transfer coefficient, and is function of the Prandtl and Grashof numbers given in equations (2.4) and (2.5).

The last mode of heat transfer is thermal radiation. It is defined as the radiant energy emitted by a medium, which is solely due to its temperature.

The wavelength range encompassed by thermal radiation is approximately 0.1 - 100μm, and visible light in the range 0.35 - 0.75μm.

According to the second law of thermodynamics, there is a maximum amount of radiant energy which can be transmitted at a given temperature and wavelength. A black body is defined as being a body which emits this maximum radiation. The quantity $e_{b\upsilon}$ is termed the monochromatic emissive power of a black body. This is a function of frequency, υ, and absolute temperature, T, of the body. The explicit form of $e_{b\upsilon}(T)$ is given by Planck's law [6],

$$e_{b\upsilon}(T) = \frac{2\,\pi\,h\,\upsilon^3 m^2}{c^2\left(\,e^{(h\upsilon/\kappa T)}-1\,\right)} \qquad (2.12)$$

where h is Planck's constant,
κ is Boltzmann constant,
m is the refraction index,
c is the speed of light,
and T is the absolute temperature.

The total black body emissive power is denoted by e_b. This represents the energy emitted over all frequencies and is given by,

$$e_b(T) = \int_0^\infty e_{b\upsilon}(T)\;\partial\upsilon \qquad (2.13)$$

Substituting equation (2.12) into the above gives,

$$e_b(T) = m^2\sigma T^4 \qquad (2.14)$$

where

$$\sigma = \frac{\pi^5\kappa^4}{15c^2h^3} \qquad (2.15)$$

and is called the Stefan-Boltzmann constant.

This is conveniently expressed for m=1, but must be taken into account when dealing with black body radiation into adjacent media within which m≠1. Real surfaces generally emit less energy than black bodies, and the monochromatic hemispherical emittance ε_λ is defined as the ratio of e_λ to $e_{b\lambda}$, where both

quantities are taken at the same wavelength λ and temperature. Total radiation across all frequencies, e, is given by,

$$e = \int_0^\infty e_\lambda \, \partial\lambda = \int_0^\infty \varepsilon_\lambda e_{b\lambda} \, \partial\lambda$$

$$= \varepsilon \, \sigma \, T^4 \qquad (2.16)$$

where

$$\varepsilon = \frac{e}{e_b} \qquad (2.17)$$

and is termed the emissivity. This depends on the material, surface conditions, i.e. roughness, and in some cases grain structure.

The radiation striking a body may be absorbed, reflected or transmitted through the body. Transmission is usually neglected as most solid bodies do not transmit radiation. For general engineering usage, the net radiative heat flux between two surfaces, neglecting absorption and reflection, is described by,

$$q = \varepsilon \, F \, \sigma \, (T^4 - T_o^4) \qquad (2.18)$$

where F is the view factor.

The above relations describe radiation leaving or striking a surface, and are not applicable for absorbing, emitting and scattering materials such as lightweight fibrous insulations. Heat transfer through these materials is by conduction, convection and radiation. The relative importance of the different modes depends on the material properties and operating conditions, though convective transfer is often neglected. Mathematical relations describing this complex heat transfer are given by Sparrow and Cess [7] and Viskanta [8]. These equations are written in terms of several parameters which need to be experimentally determined, e.g. conductivity, emissivity, absorption-, scattering- and extinction coefficients, optical thickness, etc. Sparrow and Cess [7] define a parameter N which measures the relative importance of conduction and radiation in the overall heat transfer. This parameter is given by,

$$N = \frac{K\beta}{4\sigma T^3} \qquad (2.19)$$

where K is the conductivity,

ß is the extinction coefficient and

T is the absolute temperature.

Pure conduction takes place when N = ∞, and pure radiation when N = 0. Values in between give a measure of the relative importance of the conduction and radiation transfer modes.

2.3 Problems Associated to the Casting Process

Casting defects can be broadly described as discontinuities in structural and compositional homogeneity, which reduce the mechanical properties of the casting. The major defects are voids, hot tears, porosity and segregation.

Most metal, cast iron being an exception, contract during solidification. Liquid metal has to be fed into the solidifying area to compensate for this solidification shrinkage. Campbell [9] proposed a feeding model with four modes occurring at different stages of solidification. Figure 2.8 shows the four feeding modes within a casting.

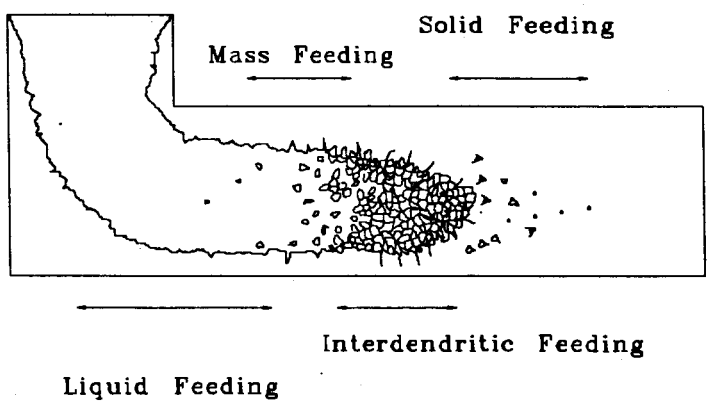

Figure 2.8 Schematic representation of four feeding mechanisms

Liquid feeding occurs in the early stages of solidification. Mass feeding takes the form of semi-solid precipitates suspended in the liquid. Interdendritic feeding occurs within the mushy region. The last mode is solid

feeding which takes place during the latter stage of solidification and is associated with distortion.

2.3.1 Voids and Hot Tears

A complete lack of liquid feeding results in void formation. This generally occurs in regions where liquid metal is surrounded by solidifying metal, with no access to further liquid reserves. There is insufficient liquid available to compensate for shrinkage and a void is formed.

Hot tears occur when coherent semi-solid regions are surrounded by contracting solid metal. The tensile stresses applied on the weak semi-solid result in large strains, and tearing occurs when strain limits are exceeded.

2.3.2 Porosity

Porosity formation is attributed to failure of interdendritic feeding. A relationship in terms of interdendritic fluid flow, shrinkage and porosity growth can be obtained by applying the conservation of mass principle to a small volume element within the mushy zone. This relationship is given by,

$$\left(\frac{\rho_S}{\rho_L} - 1\right)\frac{\partial f_L}{\partial t} - \mathbf{v}\cdot\nabla f_L + \frac{\partial f_P}{\partial t} = 0 \qquad (2.20)$$

where ρ_S and ρ_L are the liquid and solid densities,
$\mathbf{v}$ is the interdendritic flow field,
f_L and f_P are the liquid and porosity fractions.

The above three terms represent shrinkage, interdendritic fluid flow contribution and porosity formation respectively. From this equation it can be seen that porosity occurs when interdendritic feeding is insufficient to compensate for solidification shrinkage. The interdendritic flow is severely impeded by the developing semi-solid and a drop in pressure results. The local pressure within the mushy zone can be expressed as follows,

$$P(y) = \rho_L g_r y - \Delta P$$

where $\rho_L g_r y$ is the hydrostatic pressure and

ΔP is the pressure drop in the interdendritic channels due to flow resistance.

Microporosity occurs when the local pressure drops below a critical value, which may be predicted using nucleation theory. Lecomte-Beckers [10] proposed a microporosity index ΔP^*, which approximates this pressure drop in a directionally solidifying casting.

$$\Delta P^* = \frac{24\ \mu\ \hat{\beta}\ n\ \mathcal{T}^3}{\rho_L g}\left(\frac{\Delta T_m}{G}\right)\left(\frac{\partial f_s}{\partial t}\right)$$

where $\hat{\beta} = \dfrac{\rho_L - \rho_S}{\rho_L}$ is a solidification shrinkage parameter,

μ is viscosity,

n is the number of interdendritic channels,

$\mathcal{T}$ is the dendrite *tortuosity* which estimates the importance of secondary dendrite arms,

G is the thermal gradient,

ΔT_m is the alloy solidification temperature range.

This parameter indicates that material integrity is favoured by a short solidification range, low dendrite number density and tortuosity, solidification rate, and high residual liquid density, fluidity and thermal gradient. Although this parameter is defined strictly for directional solidification, it can be used to measure the likelihood of porosity defects in equiaxed castings.

2.3.3 Segregation

The gradient in solute concentration, observed in castings, is termed segregation. This occurs on both the dendrite arm scale, microsegregation, and larger scale, macrosegregation.

Microsegregation applies to a region of the size of a dendrite arm. Flemings [4], derived a simplified equation for compositional variation within a tiny region, the size of a dendrite arm, during dendritic solidification. This is given below.

$$C_s^* = k\, C_0 [\, 1 - f_s]^{(k-1)}$$

where $C_s^* = k\, C_L^*$ is the solid composition at the liquid-solid interface after f_s solid fraction has formed.
C_0 is the initial composition,
k is the equilibrium partition ratio determined by the phase diagram.

This equation demonstrates the variation of local composition as a function of local solidification progress. This microscale composition gradient constitutes microsegregation.

Macrosegregation is caused by the displacement of the highly segregated phases present in the mushy region. These are transported by interdendritic and bulk fluid flow. Typical ingot casting with macrosegregation defects is shown in figure 2.9 [4].

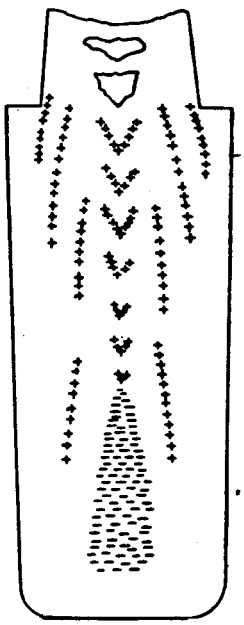

Figure 2.9 Macrosegregation in a steel ingot. Positive and negative signs indicate positive and negative segregation respectively.

Consider a volume element in the interdendritic fluid, and assume negligible solid motion. The conservation of solute mass produces the following

relation,

$$\frac{\partial}{\partial t}(\bar{\rho}\ \bar{\mathbb{C}}) = -\nabla\cdot\rho_L f_L \mathbb{C}_L \mathbf{v}$$

where $\bar{\rho}$ and $\bar{\mathbb{C}}$ are the average density and composition respectively. This may be rewritten [4] as,

$$\frac{\partial f_L}{\partial \mathbb{C}_L} = -\left(\frac{1-\beta}{1-k}\right)\left(1 + \frac{\mathbf{v}\cdot\nabla T}{\hat{T}}\right)\frac{f_L}{\mathbb{C}_L}$$

where $\frac{\partial f_L}{\partial \mathbb{C}_L}$ is the derivative of liquid fraction with respect to composition,
and $\hat{T}$ the local temperature change.

The above equation is for the generalized three dimensional heat and fluid flow condition, assuming constant solid density during solidification, negligible net solute change through diffusion, and no pore formation. It describes the influence of fluid flow on liquid and solid composition. The equation gives the local composition of the liquid in the casting. This equation is used in conjunction with Darcy's law of fluid flow through porous media, equation (2.7), to quantitatively describe macrosegregation.

3. Overview of Numerical Modelling of Solidification

Phase changes occur in a large number of physical problems and pose a significant challenge to the analyst. The first attempt at solidification modelling was published by Stefan, studying ice formation. The phrase, *Stefan problem*, has since been used to describe any general freezing problem. The governing equations for the simple one dimensional Stefan problem can be written as,

$$\frac{\partial}{\partial x}\left[K_s \frac{\partial T_s}{\partial x}\right] = \rho_s C_s \frac{\partial T_s}{\partial t} \quad \text{for the solid phase,}$$

and (3.1)

$$\frac{\partial}{\partial x}\left[K_L \frac{\partial T_L}{\partial x}\right] = \rho_L C_L \frac{\partial T_L}{\partial t} \quad \text{for the liquid phase,}$$

with conditions at the solid-liquid interface $x = S(T,x)$,

$$T_L = T_s = T_M$$

$$K_L \frac{\partial T_L}{\partial x} - K_s \frac{\partial T_s}{\partial x} = -\rho_s L \frac{dS(T,x)}{dt}$$

where K is conductivity,
L is latent heat of fusion,
ρ is density,
C is specific heat,
S defines the interface position, at the liquid-solid interface,
subscripts L and s represent liquid and solid properties respectively.

Latent heat of fusion is liberated at the solid-liquid interface, with the thermal properties of the two phases usually differing. This presents a nonlinear heat conduction problem with a moving boundary, and has few closed form solutions.

3.1 Analytical Methods

Neumann [11] presented the first closed form analytical solution for the phase change problem. This solution provides the temperature distribution for a

semi-infinite region $x > 0$, initially at a constant temperature above the materials melting point, and surface temperature at $x = 0$ set to zero at time $t = 0$. Other solutions are also available for prescribed surface temperature conditions. Consider two simple analyses of an ingot casting, assuming one dimensional heat flow with the mould either at constant temperature, figure 3.1(a), or very thick, figure 3.1(b),,and negligible thermal impedance at metal-mould interface. The temperature distribution for both cases are illustrated in figure 3.1 [4].

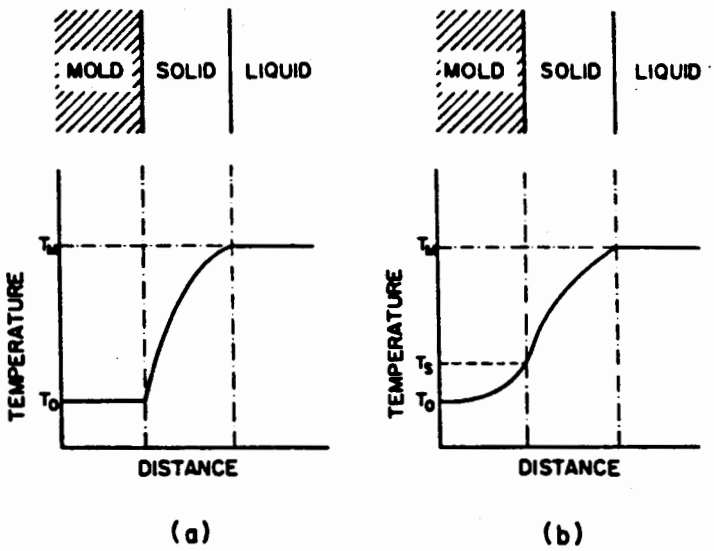

Figure 3.1 Temperature profile for solidification against a flat mould (a) at a constant temperature and (b) very thick with outside temperature constant.

Solutions to both problems are governed by the partial differential equation

$$\alpha \frac{\partial^2 T}{\partial x^2} = \frac{\partial T}{\partial t} \tag{3.2}$$

and subject to,

$$K_s \left(\frac{\partial T}{\partial x} \right)_{x=S} = \rho_s L \frac{\partial S}{\partial t}$$

at the solid-liquid interface. The boundary conditions for the constant temperature mould are,

$$T = T_o \qquad \text{at } x = 0$$

$$T = T_m \qquad \text{at } x = S$$

where $\alpha = \frac{K}{\rho C}$ and is termed diffusivity,

T_m is the melting temperature.

Carslaw and Jaeger [11] give the result,

$$S = 2 \gamma \sqrt{\alpha_s t} \tag{3.3}$$

where γ is determined by

$$\gamma \, e^{\gamma^2} \operatorname{erf} \gamma = (T_m - T_0) \frac{C_s}{L \sqrt{\pi}} \tag{3.4}$$

The temperature distribution in the solidifying metal given by

$$\frac{T - To}{To^* - To} = \operatorname{erf} \frac{x}{2\sqrt{\alpha_s t}} \tag{3.5}$$

where C_s is the specific heat of the solid metal,

To^* is an integration constant.

and the error function $\operatorname{erf}(\phi)$ is defined by

$$\operatorname{erf} \phi = \frac{2}{\sqrt{\pi}} \int_0^{\phi} e^{-\zeta^2} d\zeta$$

The solution for the semi-infinite mould is similar with γ defined by

$$\gamma \, e^{\gamma^2} \left(\sqrt{\frac{K_s \rho_s C_s}{K_m \rho_m C_m}} + \operatorname{erf} \gamma \right) = (T_m - To) \frac{C_s}{L \sqrt{\pi}} \tag{3.6}$$

and temperature distribution becoming

$$\frac{T - Ts}{To^* - Ts} = \operatorname{erf} \frac{x}{2\sqrt{\alpha_s t}} \tag{3.7}$$

where Ts is the temperature of the metal-mould interface.

Chvorinov's rule is an empirical formula used by foundry personnel to predict a castings solidification time using its ratio of volume to surface area.

This can be derived from equation (3.2), assuming all sections of the mould surface have equal ability to absorb heat, regardless of interface position or contour. Thus interface position S can be replaced by V_s/A, where V_s is the volume solidified at time t and A is the area of the metal-mould interface. When solidification is complete

$$\frac{V}{A} = 2 \gamma \sqrt{t_f}$$

where t_f is the total solidification time. Equation 3.3 shows that γ is a constant determined by material properties and mould temperature. Thus

$$t_f = a \left(\frac{V}{A}\right)^2 \qquad (3.8)$$

with $a = 4 \gamma^2$. This states that total solidification time is proportional to the square of the castings volume to surface area ratio. This relationship is useful for initial estimates of total solidification time.

Unfortunately the analytical solutions are only available for simple geometries and boundary conditions, and thus not applicable for general casting geometries and boundary conditions. However, the analytical solutions for simple problems can be used to benchmark numerical schemes and determine their accuracy.

3.2 Numerical Methods

Numerical methods, usually finite difference or finite element methods [12], are used to model complex castings. The casting and mould are replaced by a grid, or mesh of elements and nodes. Temperatures are calculated at these nodes and the castings temperature field is approximated piece wise by these nodal values. Temperatures between nodes can be obtained by interpolation. The latent heat released during solidification, at the liquid solid interface, is difficult to model directly using numerical methods and various indirect techniques are used. Three methods are described below.

The temperature recovery method is probably the simplest. The temperature distribution is first calculated without considering latent heat effects. For discrete isothermal phase changes, the nodal temperatures at the

solidification interface is set back to the phase change temperature, and an equivalent amount of heat is added to a nodal enthalpy budget. These nodal temperatures are kept constant until the enthalpy budget balances the latent heat. When considering materials which solidify over a temperature range [13], the temperature T of the solidifying node is set to,

$$T = T_L - \left(\frac{\Delta H}{L}\right)\Delta T_m \tag{3.9}$$

where T_L is the liquidus temperature,
ΔH is the value of the enthalpy budget,
L is the latent heat of fusion,
ΔT_m is the solidifying temperature range.

The apparent capacity method takes the latent heat into account by increasing the metal's specific heat capacity within the solidification temperature range, to account for the latent heat released. The apparent capacity C_a is given by,

$$\begin{aligned} C_a &= C_s && T < T_s \\ C_a &= C_m + \frac{L}{T_L - T_S} && T_s \leq T \leq T_L \\ C_a &= C_L && T > T_L \end{aligned} \tag{3.10}$$

assuming linear latent heat release, where C_m is the average of the liquid and solid specific heat capacities C_L and C_s respectively.

The specific heat function defined above in equation (3.10), behaves as dirac delta type function during the phase change. This presents stability and convergence difficulties when implemented in numerical modelling techniques. The enthalpy method reduces this problem by formulating the governing equation in terms of enthalpy, H, which has a smoother transition during solidification, as shown in figure 3.2, and implicitly models the latent heat released.

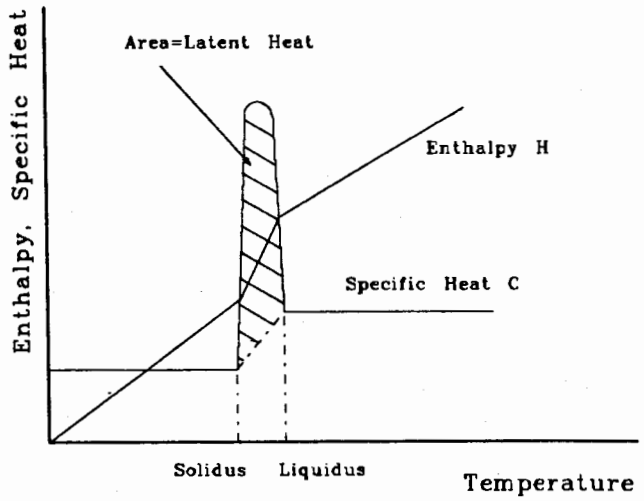

Figure 3.2 Specific heat and enthalpy variations during solidification.

The transient heat conduction equation becomes,

$$\nabla \cdot K \nabla T + Q = \rho \frac{\partial H}{\partial t} \tag{3.11}$$

where enthalpy refers to a materials heat content and is given by,

$$H(T) = \int_{T_{ref}}^{T} C\,(T)\, dT$$

where C is the specific heat of the metal, and is defined by equation (3.10) for linear heat release.

The above are three examples of the various techniques which are implemented in numerical methods, to account for the latent heat which is released during solidification. The finite difference and finite element methods are the two most commonly used numerical methods in the field of solidification modelling.

3.2.1 Finite Difference Method

The problem domain is approximated by a number of discrete points called nodes arranged in a grid formation. The finite difference method uses direct approximations of the partial derivatives at these nodes to solve the

governing differential equation. The finite difference approximations of the partial derivatives $\partial\phi/\partial x$ and $\partial^2\phi/\partial x^2$ of the function ϕ, can be derived using Taylors series expansion for $\phi(x+\Delta x)$ and $\phi(x-\Delta x)$, and neglecting certain higher order terms. The resulting approximations are classified according to their order of accuracy, and given in table 3.1.

Derivative	Difference approximation	Order of accuracy
$\frac{d\phi}{dx}$	$\frac{\phi_{j+1} - \phi_j}{\Delta x}$ (forward)	$O(\Delta x)$
	$\frac{\phi_j - \phi_{j-1}}{\Delta x}$ (backward)	$O(\Delta x)$
	$\frac{\phi_{j+1} - \phi_{j-1}}{2\Delta x}$ (central)	$O(\Delta x)^2$
	$\frac{\phi_{j-2} - \phi_{j-1} + \phi_{j+1} - \phi_{j+2}}{12\Delta x}$ (central)	$O(\Delta x)^4$
$\frac{d^2\phi}{dx^2}$	$\frac{\phi_{j-1} - 2\phi_j + \phi_{j-1}}{(\Delta x)^2}$	$O(\Delta x)^2$
	$\frac{\phi_{j-2} - 16\phi_{j-1} - 30\phi_j + 16\phi_{j+1} - \phi_{j+2}}{12(\Delta x)^2}$	$O(\Delta x)^4$

Table 3.1 difference approximations for first and second derivatives of function ϕ.

Rewriting the governing equations in terms of these approximations at each node leads to a set of simultaneous equations in terms of nodal temperatures. Consider a two dimensional transient heat conduction problem without heat generation, as an example. The governing equation is given by equation (2.3), neglecting the heat generation term. This can be rewritten in terms of nodal temperatures using second order central difference equations for $\partial^2T/\partial x^2$ and $\partial^2T/\partial y^2$, and a first order forward difference equation for $\partial T/\partial t$.

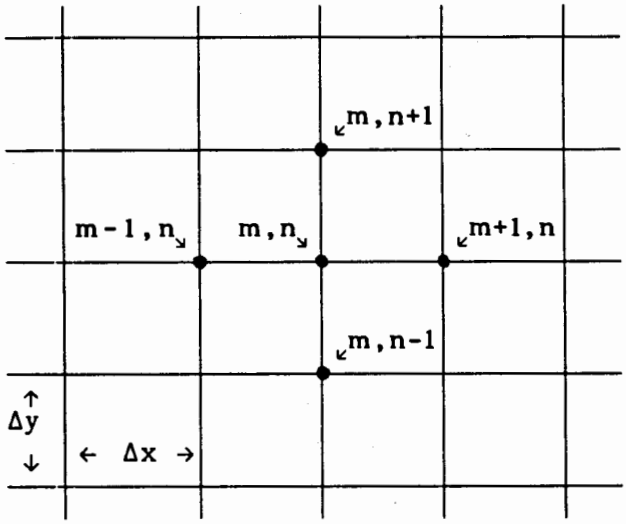

Figure 3.3 Nomenclature for finite difference solution of two dimensional transient conduction problem.

Using a regular mesh with $\Delta x = \Delta y = l$, as shown in figure 3.3, and introducing the Fourier number, $Fo = \frac{\alpha \Delta t}{(\Delta l)^2}$, the explicit form of the equation for internal nodes becomes

$$T^{P+1}_{m,n} = Fo\left(T^{P}_{m+1,n} + T^{P}_{m-1,n} + T^{P}_{m,n+1} + T^{P}_{m,n-1}\right) + \left(1 - 4(Fo)\right)T^{P}_{m,n} \qquad (3.12)$$

where subscripts m and n are nodal increments in the x and y directions respectively, and the superscript P is the time increment, e.g.

$$T^{P}_{m+1,n} = T(x+l,y,t), \qquad \text{and} \qquad T^{P+1}_{m,n} = T(x,y,t+\Delta t)$$

These equations are written for all nodes and the simultaneous equations for the nodal temperatures are solved by matrix or iterative methods. Care must be taken in the above scheme to ensure that the coefficient of $T^{P}_{m,n}$ is always non-negative, for convergence [14]. This imposes a maximum bound on the time step allowed, which is a function of nodal increment size l. The scheme is conditionally stable, with the stability criterion,

$$\Delta t \leq \frac{l^2}{4\alpha} \qquad (3.13)$$

Increasing the mesh refinement, which usually improves accuracy, decreases the usable time step. Thus many increments may be required to model a transient casting problem. This can be avoided by using a backward difference approximation for the time derivative. The nodal equation for an internal node becomes,

$$\left(1 + 4(Fo)\right)T^{P+1}_{m,n} - Fo\left(T^{P+1}_{m+1,n} + T^{P+1}_{m-1,n} + T^{P+1}_{m,n+1} + T^{P+1}_{m,n-1}\right) = T^{P}_{m,n} \qquad (3.14)$$

which is unconditionally stable. This advantage is however offset by the additional computational effort required to solve the implicit equations.

It is important to note that the above equations are considerably different for nodes at exterior and interior corners, and boundary nodes with convection or radiation conditions. The difference equations are complicated further when using an irregular grid with changing values of Δx and Δy within the domain. It is therefore advantageous to use a regular grid, and this restriction makes the finite difference method cumbersome to employ for solidification modelling of complex castings. Yet various researchers have successfully used it to model the solidification problem, e.g. [15], [16]. Lazardis [17] used the explicit difference scheme, equation (3.12), for all internal nodes sufficiently far from the moving liquid-solid interface, and modified difference schemes for nodes on either side of the interface. Four modified equations are defined for a two dimensional analysis. The exact form of these modified schemes depend on the nodal position with respect to the interface. This complex technique is considered very accurate and has been used as a basis for comparison with other numerical methods [18].

3.2.2 Finite Element Method

In the finite element method the problem domain is discretised into a mesh consisting of a finite number of elements, each of which is defined by points called nodes. The main objective is to determine the global temperature field. This is achieved by calculating the local temperature distributions within the finite elements using a set of polynomial functions in terms of their nodal temperatures. The element shape does not have to be rectangular and may be geometrically distorted, within certain limits. The elements may also have curved boundaries depending on the shape functions used. This is an advantage when modelling complex geometries, thus making the finite element method more applicable than the finite difference method for modelling complex castings. The problem is also discretised with respect to time and the finite element mesh employed may be geometrically fixed in space or else deform with time. In the latter case the deforming mesh can be used to model the changing

liquid and solid regions directly [19].

A brief description of the enthalpy formulation follows. The governing equation is given by equation (3.11).

$$\nabla \cdot K \nabla T + Q = \rho \frac{\partial H}{\partial t} \tag{3.15}$$

with initial conditions,

$$T(x,t=0) = T_o(x)$$

Two boundary conditions on separate portions of the boundary define a fixed temperature,

$$T(x,t) = T^*(x)$$

and the heat flux at the boundary,

$$K \nabla T \cdot n = - q - h_c(T - T_\infty)$$

where h_c is the surface heat transfer or convection coefficient,
q is the prescribed flux, and includes radiation transfer where applicable.

The above equation describes an initial boundary value problem. In order to solve this problem, it is discretised with respect to space and time. The above equation is reduced to an ordinary differential equation using the Galerkin method, Gradient and Divergence theorem.

$$\int_V w\rho \frac{\partial H}{\partial T} \frac{\partial T}{\partial t} dV + \int_V K \nabla T \cdot \nabla w \, dV + \int_S w\left(q + h_c(\dot{T}-T_\infty)\right) dS - \int_V wQ \, dV = 0 \tag{3.16}$$

This equation is then written in terms of integrals over individual elements, using finite element subdivision. The Galerkin approximation is used for parameters T and w in terms of polynomial or shape functions N_I. The combination of these integrals over the elements E, produces a set of nonlinear equations which can be written in terms of matrices, at any particular time t,

$$[M]\dot{T} + [K]T - F = 0 \tag{3.17}$$

where
$$M_{ij} = \sum_{n=1}^{E} \int_V \rho\, N_i N_j \frac{\partial H}{\partial T}\, dV$$

$$K_{ij} = \sum_{n=1}^{E} \int_V \nabla N_j \cdot K\, \nabla N_i dV + \sum_{n=1}^{E} \int_S h_c N_i N_j\, dS$$

$$F_j = \sum_{n=1}^{E} \int_S \left(h_c T_\infty - q\right) N_j\, dS + \sum_{n=1}^{E} \int_V Q\, N_j\, dV$$

The internal energy matrix [M] is a nonlinear function of temperature due to the function $\partial H/\partial T$. The tensors [K] and [F] are also generally functions of temperature.

Equation (3.17) can be evaluated using one of the well known trapezoidal methods for the time integration and Newtons method to solve the nonlinear equations for the temperature field. These trapezoidal methods for equation (3.17) can be written as,

$$\begin{aligned} T_{n+1} &= T_n + \Delta t\, \dot{T}_{n+\varphi} \\ \dot{T}_{n+\varphi} &= (1-\varphi)\dot{T}_n + \varphi\, \dot{T}_{n+1} \end{aligned} \tag{3.18}$$

where α is a constant, the value of which depends on which trapezoidal method, shown in table 3.2, is employed.

φ	Trapezoidal Method
0	Euler Forward Differenece
1/2	Crank-Nicholson
2/3	Galerkin
1	Euler Backward Difference

Table 3.2 Generalized trapezoidal methods.

A time step constraint may be necessary for stability depending on which

method is used. An amplification factor A can be defined for these schemes. The absolute value of A must be less than unity for stability. The amplification factor A defined for the linear case is shown below,

$$\left|\frac{(1 - (1-\varphi)\Delta t\ \lambda^h)}{(1 + \varphi\Delta t\ \lambda^h)}\right| < 1 \qquad (3.19)$$

where λ^h is the largest eigenvalue of the matrix formed by $[M]^{-1}[K]$, which can be shown to be non-negative.

When $\varphi < 1/2$ the scheme is said to be conditionally stable, and a upper bound is imposed on the allowable time step. This is expressed as,

$$\Delta t < \frac{2}{(1-2\varphi)\lambda^h} \qquad (3.20)$$

Equation (3.19) is satisfied for values of $\varphi \geq 1/2$, and thus these schemes are said to unconditionally stable. Details of the stability of transient analysis is given by Hughes and Belytschko [20]. Although the scheme is stable, the solution may oscillate if the initial time steps are too small. A minimum bound on the time increment is therefore set to prevent this oscillation phenomena. Vermeer and Verruijt [21] calculated a minimum bound for consolidation problems. The same approach is used to calculate the minimum time step for heat conduction in Appendix A.

4. Numerical Investigation of Example Problem

In view of the previous discussion, a numerical simulation of a typical casting problem was performed to determine the accuracy and feasibility of numerical methods in foundry practice. An axisymmetric wheel hub casting, shown in figure 4.1, is used for this study, as it can be analysed in two dimensions thus minimizing the computational effort.

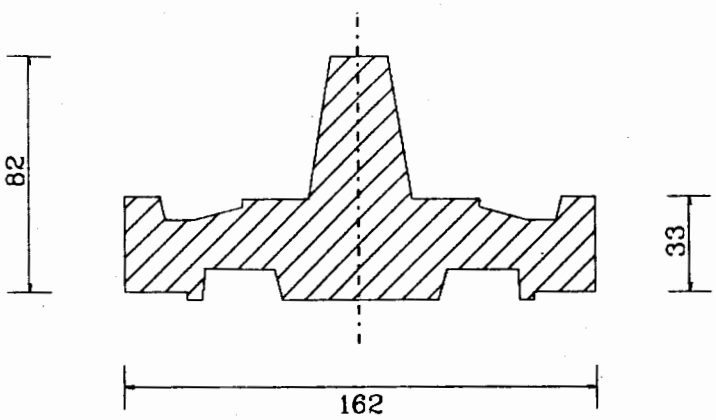

Figure 4.1 Cross section of the axisymmetric wheel hub casting. Dimensions are in millimeters.

The wheel hub is produced by the investment casting process and utilizes a ceramic shell mould, produced by the lost wax method described in section 2.1. The mould is wrapped with Koawool insulation. The layout of the mould is given in figure 4.2 below.

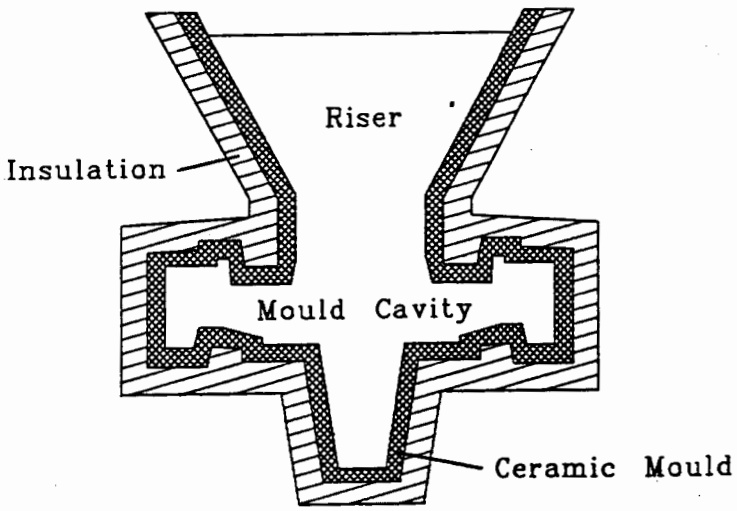

Figure 4.2 Layout of wheel hub casting mould.

The metal is a nickel based superalloy and is cast under vacuum conditions, to prevent oxidation. This takes place within a vacuum induction furnace shown schematically in figure 4.3.

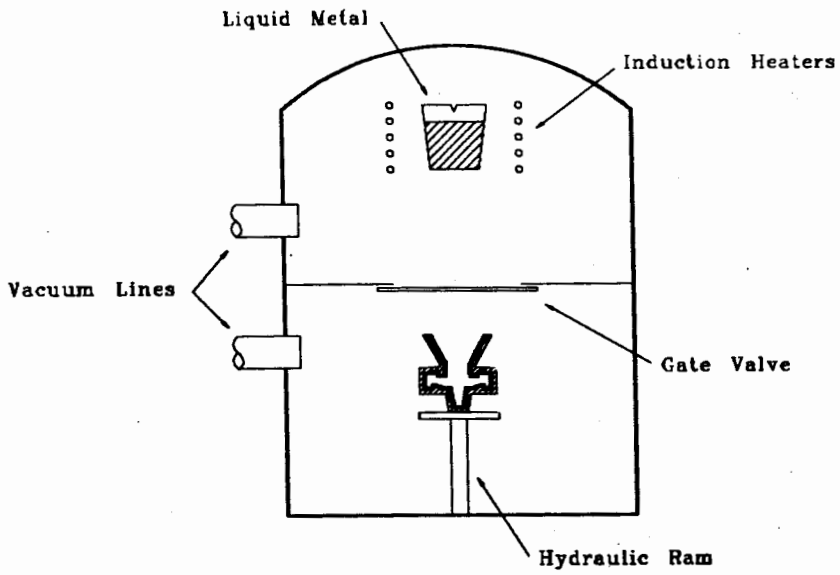

Figure 4.3 Schematic diagram of the vacuum induction furnace.

Experimental data was obtained, using instrumented castings, to compare with numerical results. These experiments were performed at the CSIR's Division of Materials Science and Technology in Pretoria.

4.1 Experimental Castings

The experimental results took the form of temperature histories at various points within the casting. Numerical work completed prior to experimental castings was used in determining thermocouple locations.

4.1.1 Instrumented Mould Layout

Due to instrument limitations only seven thermocouples could be used simultaneously, and thus two instrumented castings were carried out in order to obtain enough data. Thermocouple positions for the two castings are shown in figure 4.4. Although shown in one plane, the thermocouples where arranged

as distant as possible from each other in both castings. Numerical results obtained from preliminary studies, described in section 4.2.3, were used to determine suitable thermocouple locations.

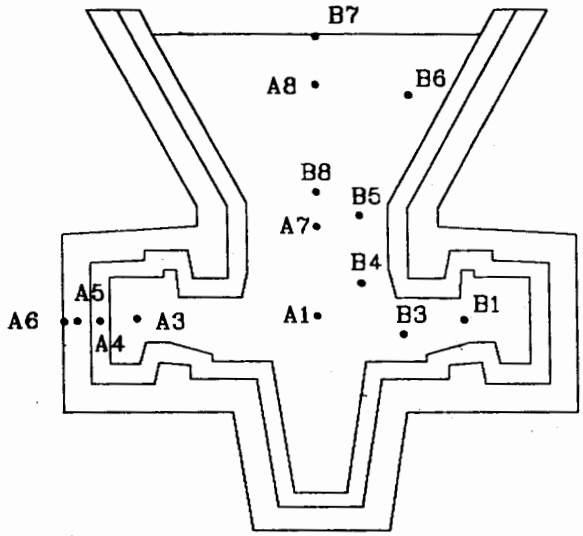

Figure 4.4 Thermocouple locations for experiment 1 and 2.

The prefixes of the thermocouple numbers, A and B, are used to differentiate between experiment 1 and 2 respectively. Due to the high pouring temperature, 1440°C, Platinum-Rhodium thermocouples are used. The thermocouple tip is protected by a ceramic shielding tube, leaving only the junction exposed. The leads are insulated with alumina beads and all fourteen thermocouple wires connected to a coupling plug, enabling a quick connection to the instrumentation.

4.1.2 Experimental Procedure

The mould is preheated and soaked in a gas fired preheating furnace at 1100°C. The metal is heated to pour temperature and the mould transferred to the vacuum induction furnace. The induction furnace has two chambers, both at vacuum conditions, and separated by a gate valve. When both the metal and mould are at the correct temperatures the lower chamber is vented and opened. The mould is transported from the preheating furnace and placed within the lower chamber on a hydraulic ram. The chamber is evacuated and the gate valve opened once an acceptable pressure value is reached. The hydraulic ram raises the mould into the upper chamber where pouring takes place. The metal is

heated to 1440°C and is poured gently to prevent the breaking the thermocouple's shielding tubes. The casting is then descended into the lower chamber, after which the gate valve is closed. The lower chamber is vented and opened, and an exothermic powder is poured over the metal surface. The casting is then left to cool within the furnace. The furnace walls are water cooled and maintained at approximately 20 - 25°C.

4.1.3 Observations

Two general points were noticed in both experiments. Firstly, swirling currents induced through pouring were visible on the metal surface. This liquid motion contributes to the overall heat transfer within the liquid metal as discussed in section 2.2.2.2.

Secondly the mould could be seen glowing through the Koawool insulation. This had not been anticipated as the Koawool was assumed opaque. Thermal conduction had been expected between the mould and Koawool, and radiation and convection at the insulation-air interface. From this observation it can be argued that since light is transmitted, thermal radiation will also be transmitted through the insulation, though a portion may be absorbed, scattered or re-emitted by the insulation. The mechanics of this transfer mode are more complex than the originally expected mechanism.

During the first experiment, thermocouple A8's shielding broke as the metal was poured and was seen floating on the metal surface. There is thus some doubt about the accuracy of this measured temperature as the thermocouple may have moved or formed a second junction. The recorded results for the first experiment are given in figure 4.5.

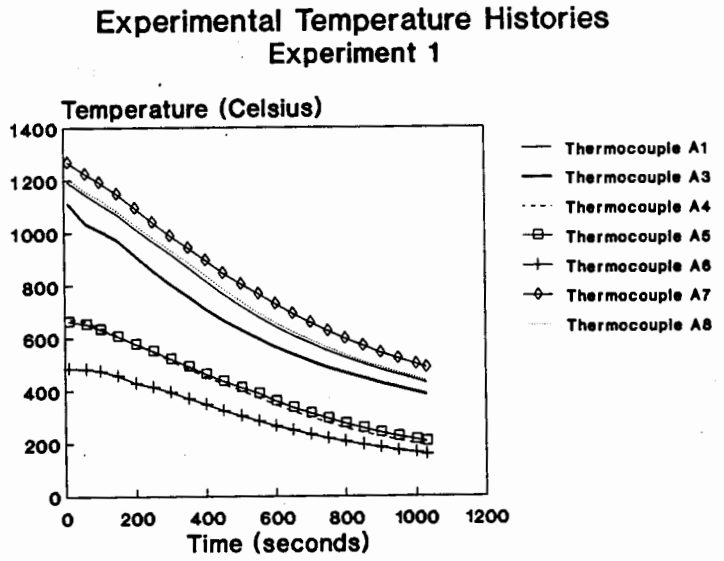

Figure 4.5 Recorded Temperature histories for experiment 1.

Due to some unknown error the recording instrument started operating about 2 to 3 minutes after pour. This was only noted later when analysing the recorded results. The temperature histories for first few minutes are therefore missing. The results also show that thermocouple A4 was recording low temperatures relative to neighbouring thermocouples A3 and A5. This was attributed to poor contact between the thermocouple and mould material.

In the second experiment another attempt was made to measure temperatures in the riser section, as a result of the thermocouple breakage in the first experiment. To avoid the imposed forces during pouring, two thermocouples, numbers B7 and B8, were inserted manually into the riser section after the exothermic powder was poured on the surface. Thermocouple B8 was pushed to the bottom of the riser, and B7 was held just below the riser surface. Thermocouple B6 broke during pouring and B8 broke soon after being inserted into the liquid metal. This was a result of thermal shock, large buoyancy forces and the brittle nature of the ceramic shielding. Thermocouples B3 and B7 broke later during the cooling stage. This was due to stress applied by solidification shrinkage and thermal contraction. The temperature histories are given in figure 4.6.

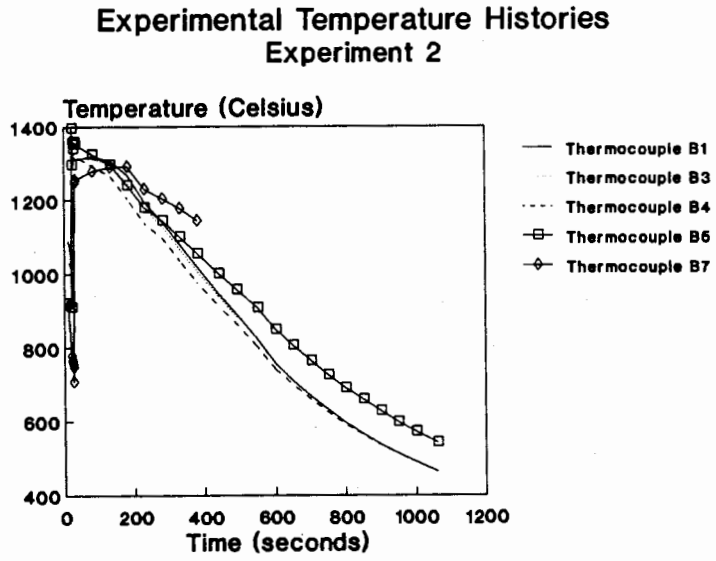

Figure 4.6 Recorded temperature histories for experiment 2.

It is noted that although the metal is heated to 1440°C prior to pouring, the maximum temperature recorded within the casting is only 1386°C. This sudden cooling may be attributed to the relatively low temperature of the mould and convection effects within the casting.

4.2 Numerical Model

Numerical modelling consists of developing a discretised mesh, defining the respective material properties, initial and boundary conditions, and implementing a numerical algorithm to calculate transient solutions. The casting is modelled on the macroscopic level as a conduction problem, ignoring liquid convection, interdendritic fluid flow and microstructural detail. Material properties are given for the nickel-based superalloy and alumina silicate mould material in Appendix B, but are not available for the Koawool insulation. Glass wool insulation values are taken from a heat transfer handbook [22] and used as an initial estimate. The finite element code ABAQUS was chosen as the numerical tool to be used in modelling the above casting problem.

4.2.1 ABAQUS Finite Element Code

The finite element code, ABAQUS, (available for research purposes at the University of Cape Town) was used as it is regarded as one of the best commercially available FEM programs for solidification analysis [23]. The code caters for 1-, 2- & 3-dimensional applications, and is also able to perform coupled thermo-mechanical analyses. The code has built in functions which make it ideal for solidification modelling. The most important of these is its ability to model the latent heat released during solidification. ABAQUS uses the enthalpy finite element formulation described in section 3.2.2. The latent heat is modelled as being linearly dissipated over the solidification temperature range. The code includes gap elements which allow the model to simulate gap formation and thermal impedance at the metal mould interface. The impedance is modelled by an average interfacial heat transfer coefficient, as described earlier by equation (2.10), which is termed gap conductance. Material and thermal properties can be entered as fixed or temperature dependent values. Boundary conditions can be prescribed as a heat flux, radiation, convection or a combination of the above. The heat flux can be constant, time dependent or a function of any number of criteria defined in a user subroutine. The convection and radiation boundary conditions are modelled using overall heat transfer coefficients. Convection transfer is modelled by the Neumann relationship given by equation (2.11). Radiation transfer is modelled using equation (2.18) and a radiation heat transfer coefficient, which is defined as the product of the Stefan-Boltzmann constant, emissivity and view factor.

The ABAQUS user's manual suggests using linear elements when modelling phase changes, as this results in a diagonalized internal energy, or heat capacity matrix [M] as defined by equation (3.17), which improves the stability for phase change problems. The Euler backward difference scheme, which is unconditionally stable, is used for the time integration. The solution may oscillate during the initial time steps and a constraint has to be applied for the initial time steps. This constraint defines the initial time step limit, as a function of material properties and element length. The derivation of this relationship is shown in Appendix A.

$$\Delta t \geq \frac{\rho C l^{2}}{6K} \qquad (4.1)$$

where ρ is the density
C is the specific heat
l is the element length
K is the thermal conductivity.

ABAQUS provides the facility of producing isothermal plots. These show the solidification front progression, size and shape of the mushy zone and can be used to predict porosity and void defects. Thermal histories for specified nodes can be plotted directly or written to file. This stored data can later be accessed and manipulated to produce estimates of thermal gradient, solidification rate, or merged with experimental data to produce temperature history comparisons.

4.2.2 Finite Element Mesh

The choice of mesh refinement directly affects the accuracy of the solution. Increasing refinement usually improves accuracy but also increases computational effort, which is proportional to the square of the number of elements. A stage is reached where large prices are paid in computational effort for small gains in accuracy. With this in mind it is often better to begin an analysis with a crude mesh and refine the regions having large temperature gradients over a single elements. The initial mesh has 381 nodes and 386 elements, and is shown in figure 4.7.

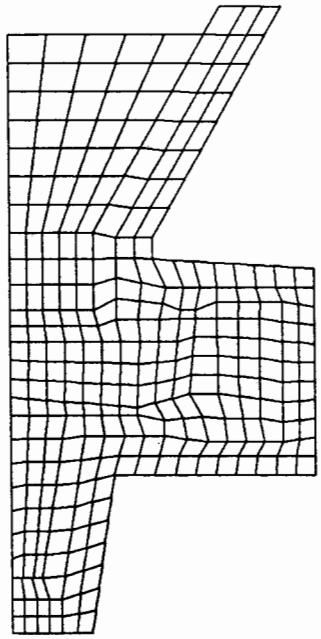

Figure 4.7 Initial finite element mesh.

The elements are 4-noded, isoparamteric axisymmetric elements. The preheating of the mould is not modelled, and the nodes within the metal and mould are set to initial temperatures of 1440°C and 1050°C respectively to simulate pouring conditions. The insulation boundary is held at a constant temperature of 20°C to model thermal radiation and convection boundary conditions, which are neglected during the initial analysis. The minimum initial time step determined by equation (4.1) is 4 seconds. Analysis results revealed that solidification progressed rapidly at the metal-mould interface during the initial time increment, due to the relatively low mould temperature. Smaller time increments are required to improve the modelling of this initial freezing, and this requires refining the mesh. A mesh sensitivity study was performed to determine a suitable level of refinement, and a parametric study to determine the solutions sensitivity to various parameters and identify those which require accurate modelling. Both these studies were performed prior to conducting the experimental castings.

4.2.2.1 Mesh Refinement Study

The lower shank portion of the wheel hub casting was used for the refinement study to minimize the computational effort. It has a simple geometry and is assumed to be representative of the whole casting. Three meshes are used for comparison. The first is equivalent to the initial mesh given in figure 4.7.

The two subsequent meshes are developed by dividing each of the previous meshes elements into four new elements. These three meshes are shown in figure 4.8.

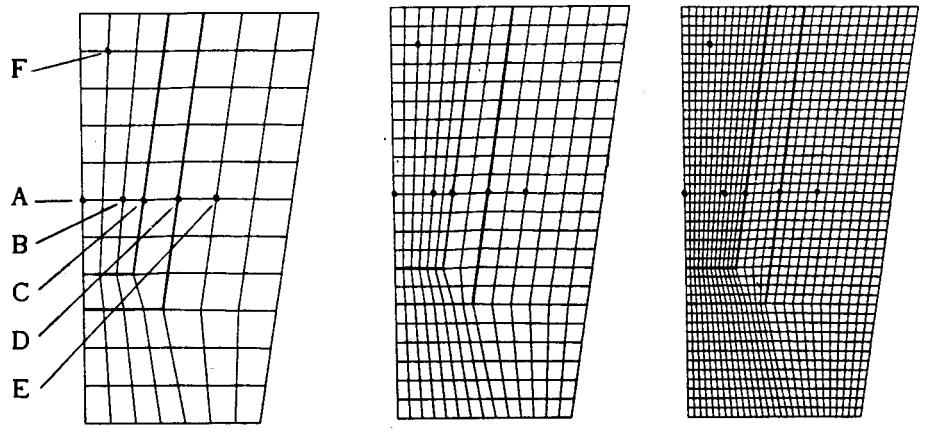

Figure 4.8 Three meshes used for mesh refinement study.

The temperature histories for the highlighted nodes in the three meshes are compared for the first five minutes of solidification to determine solution accuracy. The initial and boundary conditions are the same as those of the initial analysis. The comparison of temperature histories for node F and required CPU time are given in figure 4.9.

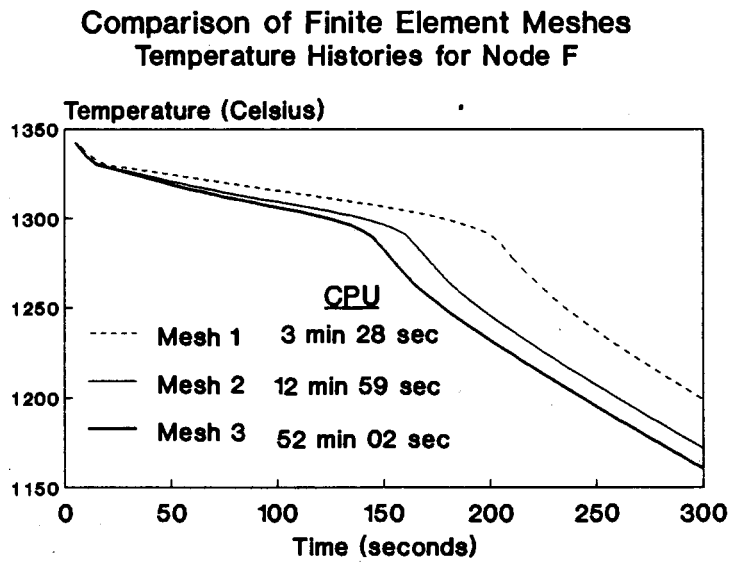

Figure 4.9 Comparison of temperature histories for node F.

From these results it was decided that mesh 2 represented a suitable compromise between computational effort and accuracy. A new finite element mesh of the casting problem, to be used in subsequent analysis, was developed using this level of refinement. This mesh, shown in figure 4.10, has 1206 nodes and 1121 elements.

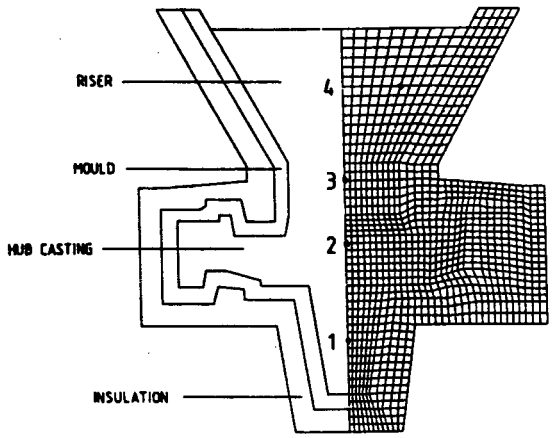

Figure 4.10 The second finite element mesh, showing nodes used for parametric study.

4.2.3 Material Properties and Boundary Conditions

In order to produce accurate results the material and boundary conditions need to be accurately modelled. In this casting problem there is some uncertainty about the properties of the Koawool, effect of the mould radiation and thermal impedance at the metal mould interface. A parametric study is performed to determine the relative significance of various parameters on the solution. Using these results a one dimensional study is conducted to obtain experimentally based approximations for the emissivity and Koawool conductivity.

4.2.3.1 Parametric Study

The question of solution accuracy arises as a result of the uncertainties in

Koawool material properties, complex boundary conditions observed during casting and thermal impedance at the metal-mould interface. A parametric study was performed to determine the models sensitivity to these various parameters and determine their influence on the overall solution. The mesh given in figure 4.10 was used with thermal radiation conditions at the mould-insulation interface, radiation and convection conditions at the insulation-air interface, and gap conductance at the metal-mould interface.

Thermal convection coefficients for the insulation-air interface are calculated using empirical equations for free convection. These calculations are shown in Appendix C. The calculated coefficients for the various surfaces range from 4.23 to 11.28 $W/m^2\ ^\circ C$. To simplify the model the surfaces are given a uniform coefficient of 10 $W/m^2\ ^0C$.

Accurate modelling of the complex radiation phenomena observed during casting requires analysis of the absorption, scattering and emitting behaviour of the Koawool insulation. These properties are not easily determined, and due to a lack of equipment and expertise, the experimental analysis necessary to measure the coefficients required for the analysis mentioned in section 2.2.2.4 was not performed. The overall effect is crudely modelled by allowing the mould-insulation and insulation-air interfaces to radiate separately through to the furnace walls, which is at 25°C. The absorption, emission and scattering effects within the insulation are neglected. Emissivity for Alumina is given in Holman [22], varying from 0.18 to 0.5 depending on grain size. No emissivity values are found for the Koawool insulation and it is assumed equal to that of Alumina. The emissivities of both materials are taken to be 0.3 during this study.

No material properties could be found for the Koawool insulation. Glass wool insulation properties, taken from Holman [22] (ρ = 24 Kg/m^3, K = 0.038 $W/m\ ^\circ C$, C = 700 $J/Kg\ ^\circ C$), are used to approximate the Koawool properties. Of the three properties, the conductivity is most likely to influence the numerical solution. This can be shown by performing a simple macroscopic heat balance for the whole casting. Considering the various heat sources and sinks this can be written as,

$$\left(q_{Se} + q_{La}\right)_{Metal} + \left(q_{Se} - q_{1}\right)_{Mould} + \left(q_{Se} - q_{2}\right)_{Insulation} = 0 \qquad (4.2)$$

where q_1 is the heat lost by radiation at the mould surface, and is a function of mould surface temperature.

q_2 is the heat conducted through to the outer insulation surface where it is lost by convection and radiation. This heat loss is a function of surface temperature which is dependent on the insulation conductivity.

subscripts Se and La refer to sensible and latent heat respectively.

Sensible heat is the thermal energy absorbed/rejected by a body as it is heated/cooled respectively. This is expressed by,

$$q_{Se} = - \rho \, C \, \frac{dT}{dt} \tag{4.3}$$

where ρ and C are the materials density and specific heat respectively. The insulation's sensible heat contribution, q_s, is minimal in comparison to that of the mould and metal, as it's product of density and specific heat is small (±300 times less) compared to that of the mould and metal, given in Appendix B. Thus moderate increases in insulation density and specific heat values will have little effect on the numerical results. The Koawool's thermal conductivity, however, directly effects the heat loss term q_2, and thus the overall heat transfer throughout the casting. Simulations performed using various values for ρ, C and K support this finding. The gap conductance is initially set to 10^{10} W/m^2 $^{\circ}C$, simulating perfect conduction and no impedance at the metal-mould interface.

To determine their individual effect on the solution, the emissivity, convection coefficient, insulation conductivity and gap conductance values are varied and the resultant temperature histories are compared at four nodes within the casting, shown in figure 4.10. These effects are shown in figures 4.11(a) - (e).

Influence of Mould Radiation

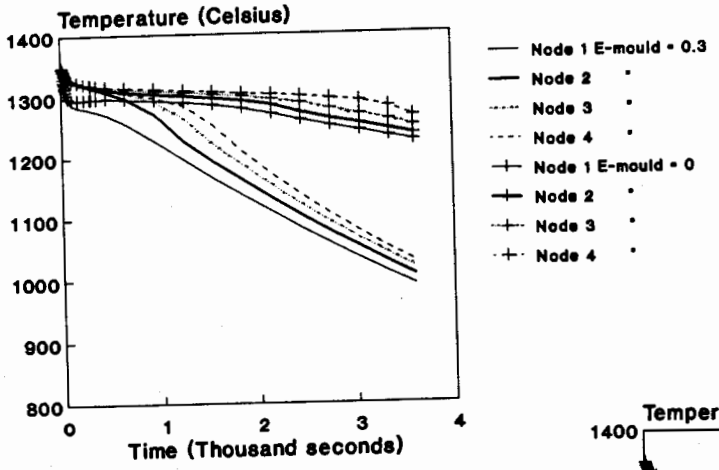

Figure 4.11 (a)

Influence of Emmissivity

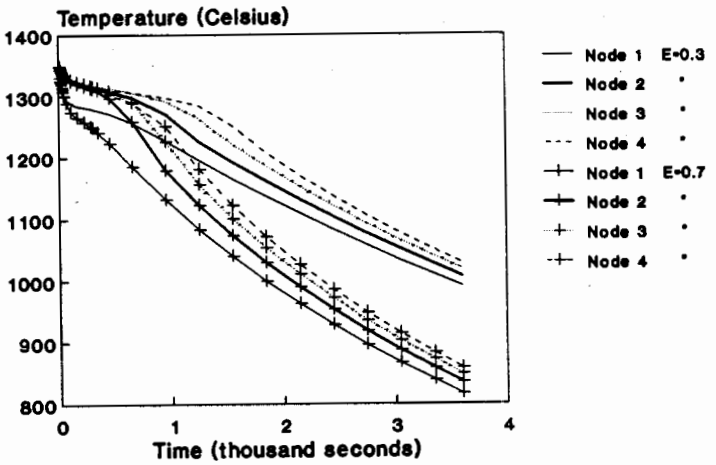

Figure 4.11 (b)

Influence of Thermal Convection

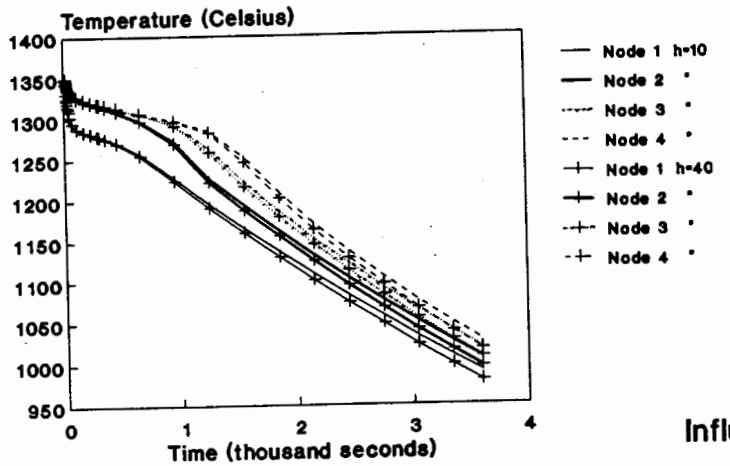

Figure 4.11 (c)

Influence of Insulation Conductivity

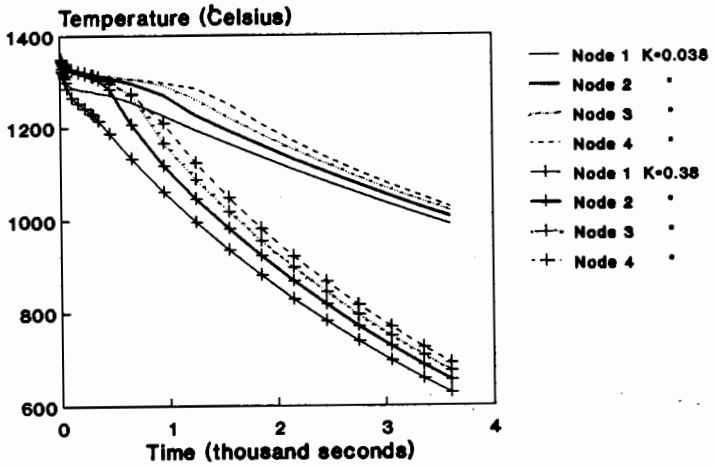

Figure 4.11 (d)

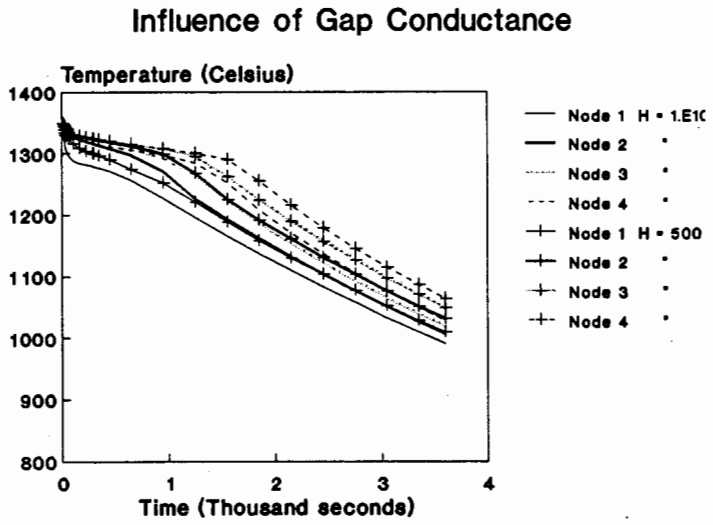

Figure 4.11 (e)

Figure 4.11 Effect of parameter variation on numerical results.

(a) Excluding mould radiation.

(b) Increasing radiation emissivity for both surfaces.

(c) Increasing convection coefficient.

(d) Increasing insulation conductivity.

(e) Decreasing metal-mould gap conductance.

Figure 4.11(a) shows the significance of modelling the mould radiation as opposed to ignoring it. It can be seen that this radiation behaviour is important and cannot be ignored. The effect of altering the emissivity for both the mould and insulation surfaces is shown in figure 4.11(b), and it is therefore important to obtain accurate values. Thermal convection is less significant and increasing the coefficient has little effect on temperature histories within the casting, as shown in figure 4.11(c). Figure 4.11(d) shows the significance of Koawool conductivity. The effect of changing the gap conductance value, in figure 4.11(e), is seen to have a reasonably small effect in comparison with variations in radiation emissivity or insulation conductivity. These results clearly show the significance of radiation behaviour and insulation conductivity. Both have large effects on the solution and need to be accurately modelled to obtain realistic results.

4.2.3.2 One-Dimensional Analysis

After the experimental castings, a one dimensional study was performed to obtain better estimates for emissivity and Koawool conductivity based on the measured data.

This is done by modelling the radial section from thermocouple positions A3 to A6, including the various radiation and convection surfaces. The emissivity and conductivity values were changed until the numerical and experimental results agreed as much as possible. The first experiment provides temperature data for the outer disc section of the casting and mould. Although the initial temperature histories after pour are not available due to the instrument malfunction described in section 4.1, the remaining data can be used for comparison with the numerical values. The heat flow in this outer disc section of the casting and mould is assumed purely radial and is simulated by a string of five one-dimensional elements from thermocouple positions A3 to A6, see figure 4.4 for these thermocouple positions. This 1-D model is shown below in figure 4.12.

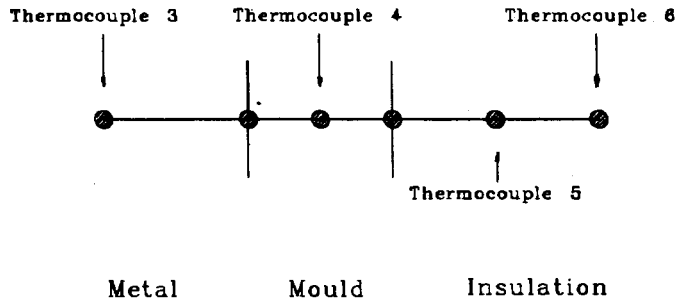

Figure 4.12 One dimensional model used to estimate emissivity and Koawool conductivity.

The temperature histories of thermocouples A3, A5 and A6 are used for comparison. The results of thermocouple A4 are discarded due to experimental error described in section 4.1. The initial temperatures are set to 1150°C, 1000°C, 600°C for the metal, mould and insulation nodes respectively. The environment temperature to which heat is lost is 25°C. The mould and insulation are given the same emissivity value due to the uncertainty of the radiation behaviour. The emissivity and insulation conductivity are changed until the resultant temperature histories resemble the experimental values.

Using this approach, the emissivity and conductivity values are estimated to be 0.5 and 0.38W/m °C respectively. This simple curve fitting method cannot be regarded as accurate, but it provides first estimates based on measured values. The advantage of using a one dimensional model is the low computational time requirements, sixty increments taking slightly less than 2 minutes of CPU time as opposed to over $1\frac{1}{2}$ hours for the complete axisymmetric model of the casting. The values obtained during this study are used in the full analysis of the casting problem, and the temperature histories compared with the second experiments recorded data.

4.2.4 Comparison of Numerical and Experimental Results

The complete casting is modelled using the mesh shown in figure 4.10, and the temperature histories are compared with Experiment 2's results.

The mould and insulation nodes are both given an initial temperature of 1050°C. Although the metal is heated to 1440°C prior to pouring, the highest recorded temperature within the casting is 1386°C and the metal nodes are therefore given an initial temperature of 1380°C. . This sudden temperature drop is due to the large temperature gradient between metal and mould, and the turbulent liquid convection occurring during and after pour. The upper metal surface is modelled as adiabatic, as it is assumed that the exothermic powder produces enough heat to compensate for heat lost by convection and radiation from its surface. The values for emissivity and Koawool conductivity obtained in the above analysis are used. The environment temperature is once again taken to be 25°C. Solidification and heat conduction are modelled for the first 1300 seconds after pour. During the initial 30 seconds the casting is under vacuum conditions and the convection condition is neglected. After this period convection is modelled using the calculated convection coefficients, given in Appendix C.

The results of the above analysis are compared to measured temperatures of Experiment 2. Temperature history comparisons for two thermocouples are given below. The overall correlation between the numerical and experimental results shown in figure 4.13 below, is good during the initial 5 minutes.

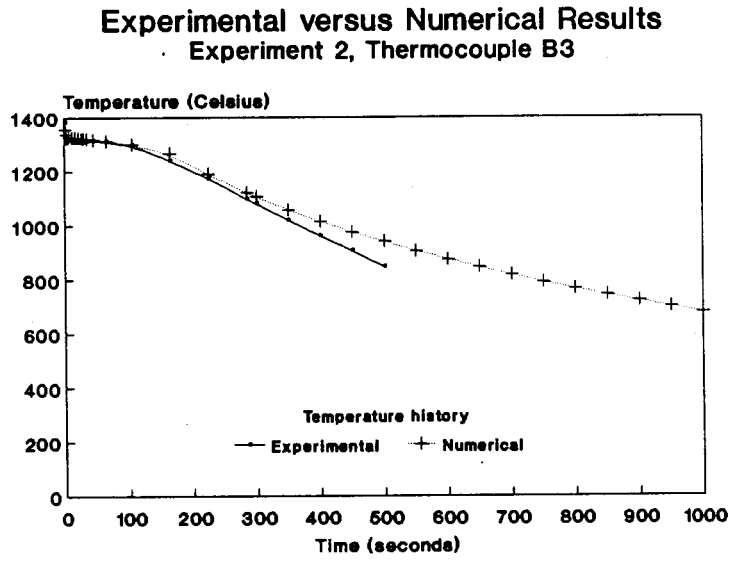

Figure 4.13 Temperature history comparison for thermocouple B3.

It is noticed, when comparing the predicted and measured temperatures, that directly after pour the measured temperature drops more rapidly than the predicted values. This sudden temperature drop is attributed to the turbulent convection occurring within the liquid and the large temperature difference, 390°C, between the metal and mould at pour. As fluid flow is not included in this model, the sudden temperature drop cannot be modelled directly. From a heat conduction point of view this convection increases the heat transferred from the metal to the mould. Harrison and Weinberg [24] showed that convection increases the overall heat transfer up to 9.6 times for liquid tin. Using this information, the effect is taken into account by increasing the liquid metal conductivity to 200 W/m°C. This improved the correlation during the initial stages after pour.

The second comparison of temperature histories is given below in figure 4.14 for thermocouple B7.

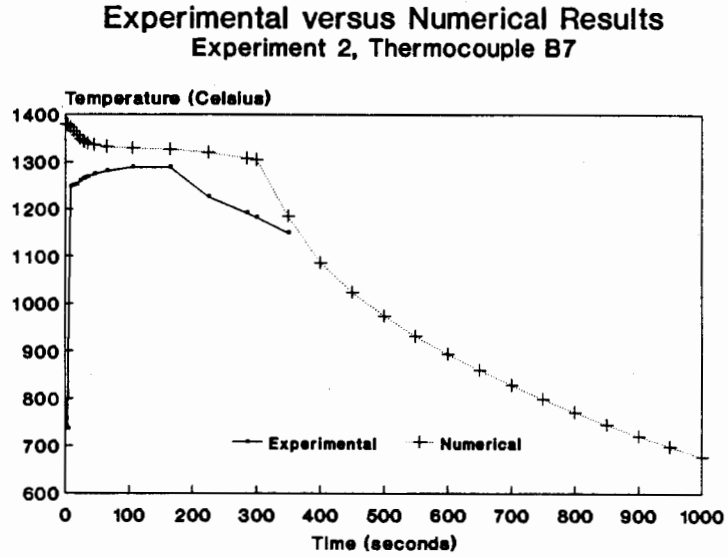

Figure 4.14 Temperature history comparison for thermocouple B7.

It can be seen that the correlation between experimental and numerical temperatures is poor. This comparison shows that the upper metal surface does not behave adiabatically as assumed. Isotherm plots using this adiabatic assumption indicate that the last region to solidify is at the metal surface. The actual location is lower down in the riser, where porosity and void defects occur in practice. The effect of the exothermic powder is thus over estimated. By considering the measured temperature history it can be seen that the exothermic powder initially absorbs energy from the metal, and the temperatures are below 1290°C. Once the chemical reaction gains momentum the temperature rises steadily to 1290°C and then drops off after approximately 160 seconds. The adiabatic assumption predicts vastly different results and is therefore not valid. In subsequent simulations the metal surface is kept at 1290°C for the first 170 seconds and then allowed to radiate with an emissivity of 0.3. This improved the correlation and can be seen in figure 4.29.

Another simulation included the thermal impedance at the metal-mould interface. Ho and Pehlke [4] calculate various gap conductance values ranging from 150 W/m^2 °C to 2.5KW/m^2 °C for different moulds. Rollett and Lewis [25] used a value of 10 KW/m^2 °C for the inner surface of a uranium hemispherical

shell casting using a graphite mould, as this interface maintains contact due to shrinkage. Thus as no values were found for a nickel superalloy and alumina mould, a conservative figure of 10 $KW/m^{2o}C$ is used for the hub casting. This impedance reduces the rate of heat transfer between the metal and mould. To maintain a reasonable correlation between experimental and numerical results the heat transfer is increased by raising the radiation emissivity from 0.5 to 0.67. This new value was arbitrarily chosen by increasing the radiation transfer coefficient (product of emissivity, Stefan-Boltzmann constant and view factor which is assumed to be unity) from 2.83×10^{-8} to 3.83×10^{-8}. The isotherm plots produced during this analysis are given in Appendix D. Two significant plots are shown below.

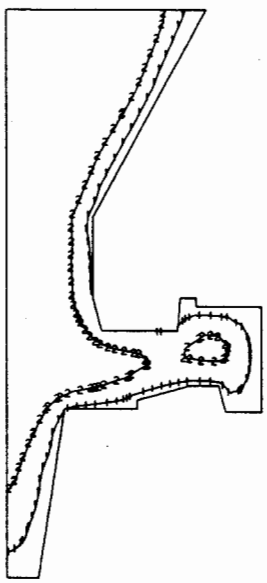

Figure 4.15 Isotherms 12 seconds after pour.

Figure 4.15 shows a fully liquid region surrounded by solidifying metal in the outer disc section of the casting. This represents a *hot spot.* Considering the second experiments thermocouple locations, the above suggests that thermocouple B1 will read slightly higher temperatures than thermocouple B3. Figure 4.16 shows a portion of the measured temperature histories for thermocouples B1 and B3, and confirms the numerical prediction.

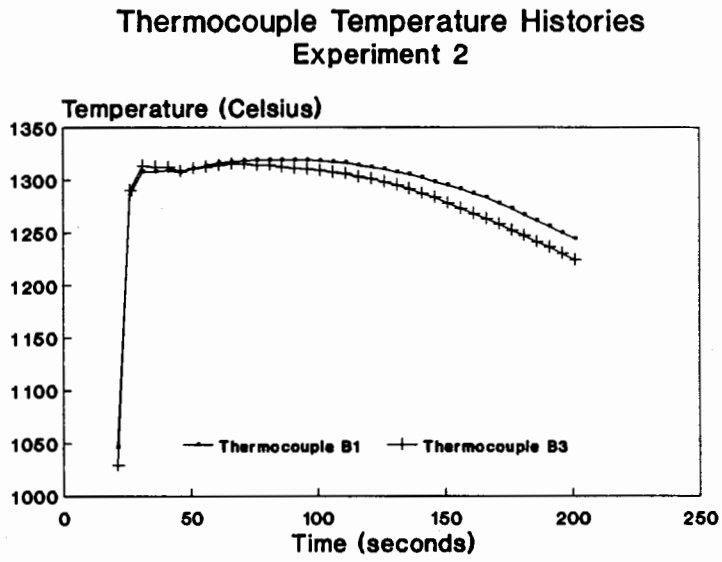

Figure 4.16 Thermocouple temperature histories for thermocouple B1 & B3, showing thermocouple B1 reading slightly higher temperatures.

The second isotherm plot shown below in figure 4.17 shows two regions likely to experience porosity and void defects.

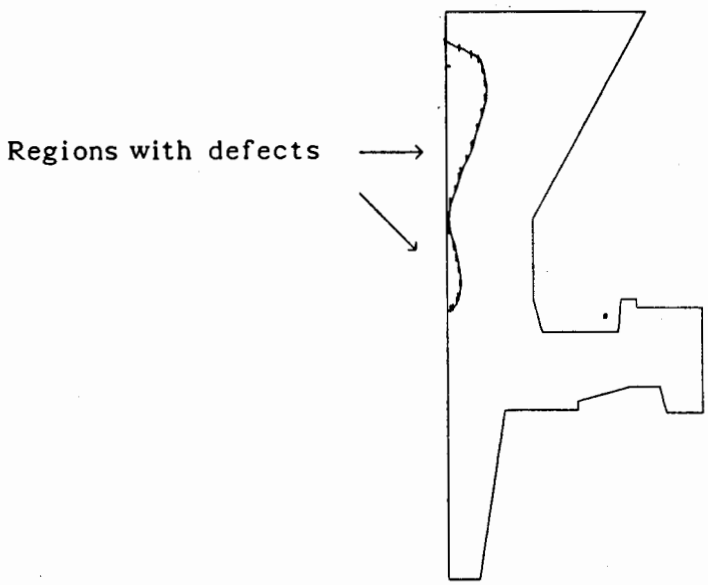

Figure 4.17 Isotherm plot showing regions likely to experience porosity and void defects.

This explains the porosity and void defect which occurs in this region. It is

important to note that this defect is not numerically predicted when the upper metal surface is modelled as adiabatic. This suggests that these defects can be avoided by improving the performance of the exothermic powder.

Comparison of numerical and experimental temperature histories for experiments 1 and 2 are given in figures 4.18 to 4.29 below. As mentioned in section 4.1.3 the initial data for experiment 1 is missing. To find a suitable time offset the measured and predicted values are compared, and a value of 155 seconds is found to give good initial agreement.

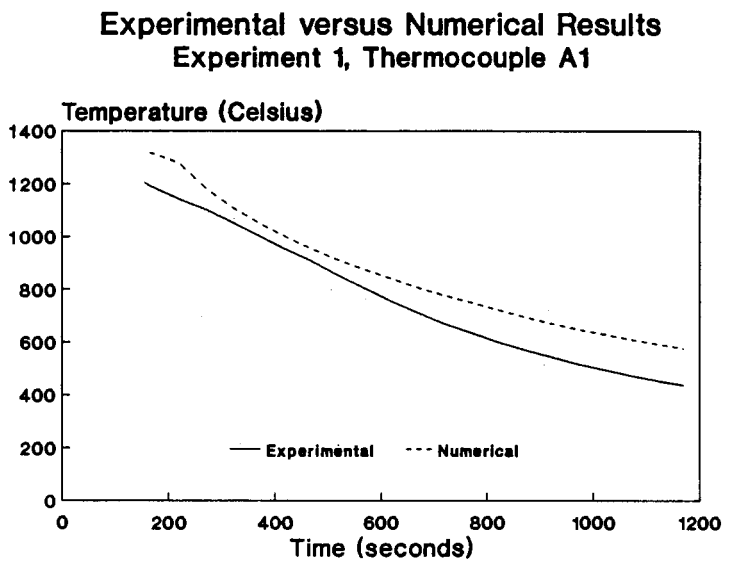

Figure 4.18 Comparison of numerical and experimental temperatures for thermocouple A1.

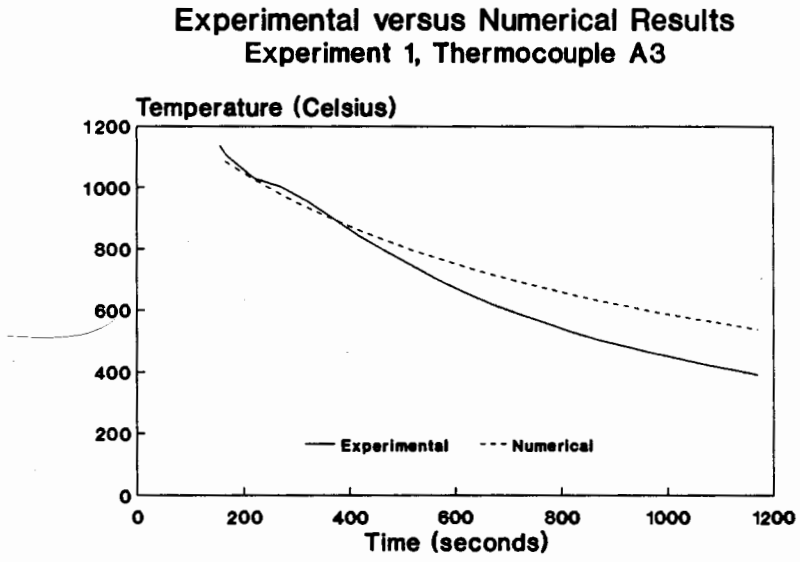

Figure 4.19 Comparison of numerical and experimental temperatures for thermocouple A3.

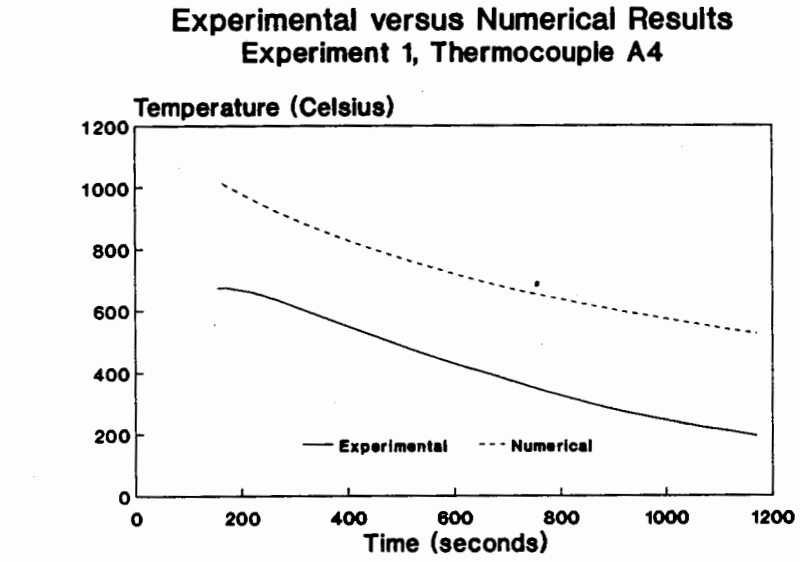

Figure 4.20 Comparison of numerical and experimental temperatures for thermocouple A4.

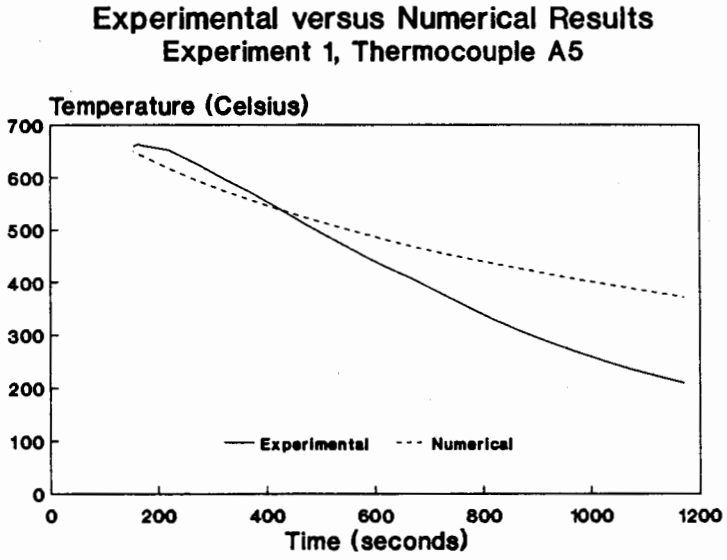

Figure 4.21 Comparison of numerical and experimental temperatures for thermocouple A5.

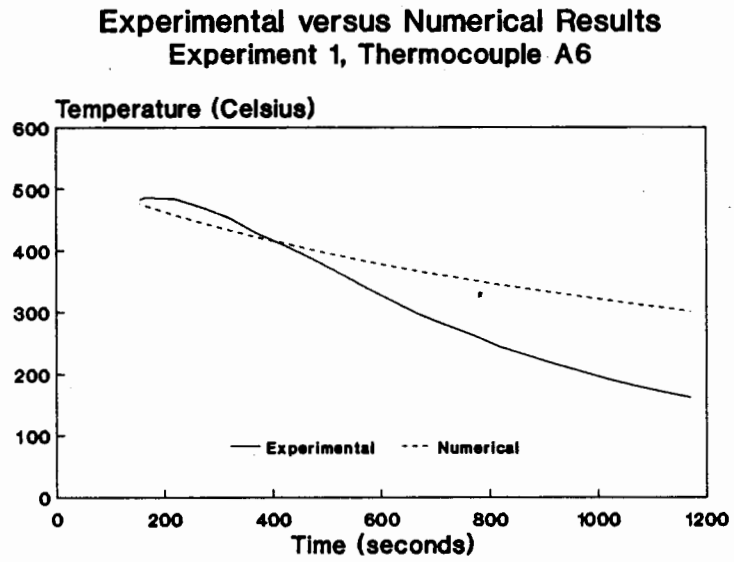

Figure 4.22 Comparison of numerical and experimental temperatures for thermocouple A6.

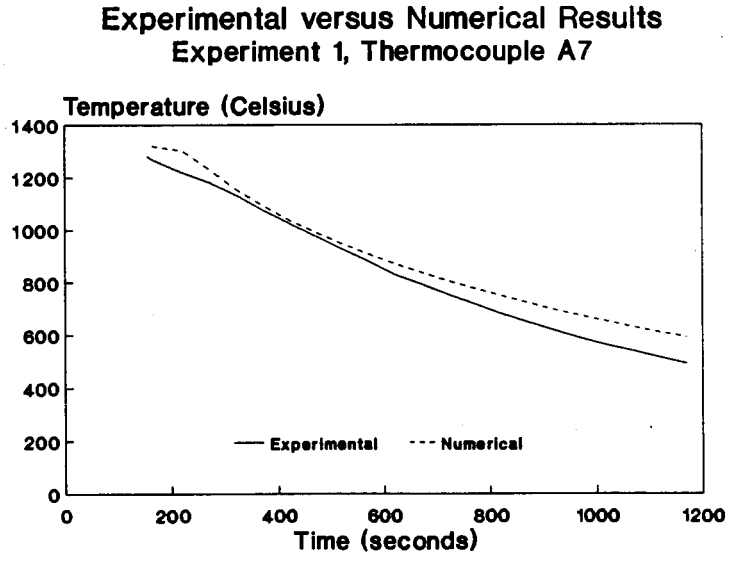

Figure 4.23 Comparison of numerical and experimental temperatures for thermocouple A7.

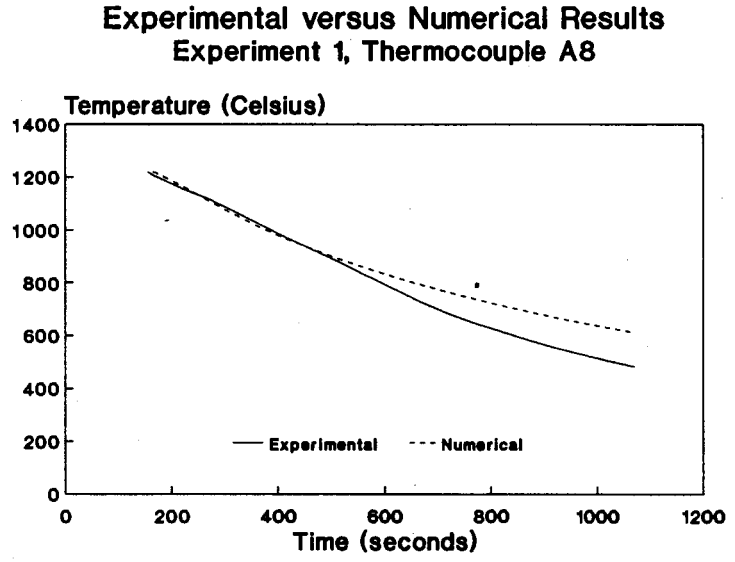

Figure 4.24 Comparison of numerical and experimental temperatures for thermocouple A8.

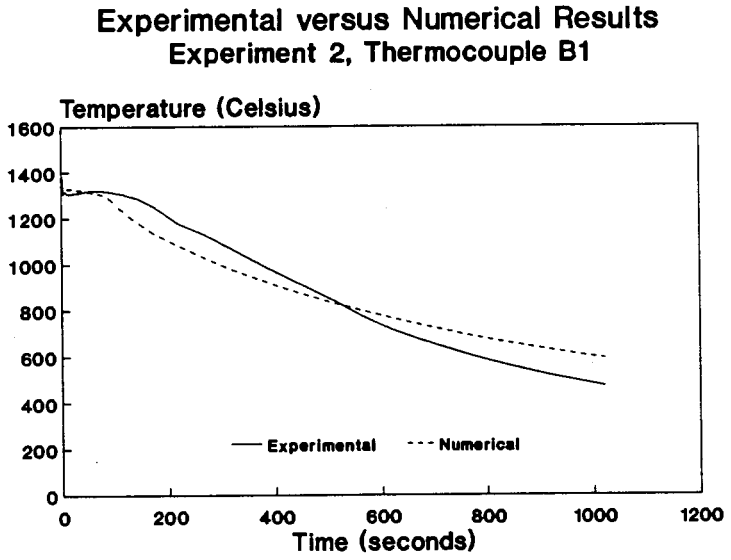

Figure 4.25 Comparison of numerical and experimental temperatures for thermocouple B1.

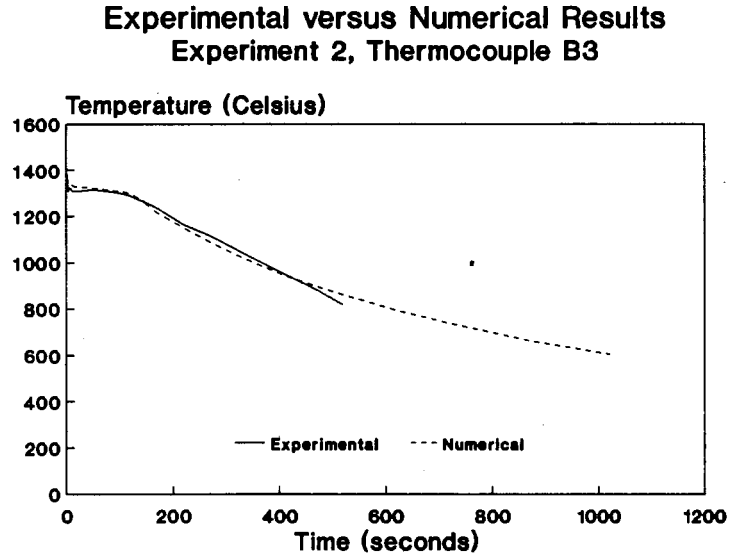

Figure 4.26 Comparison of numerical and experimental temperatures for thermocouple B3.

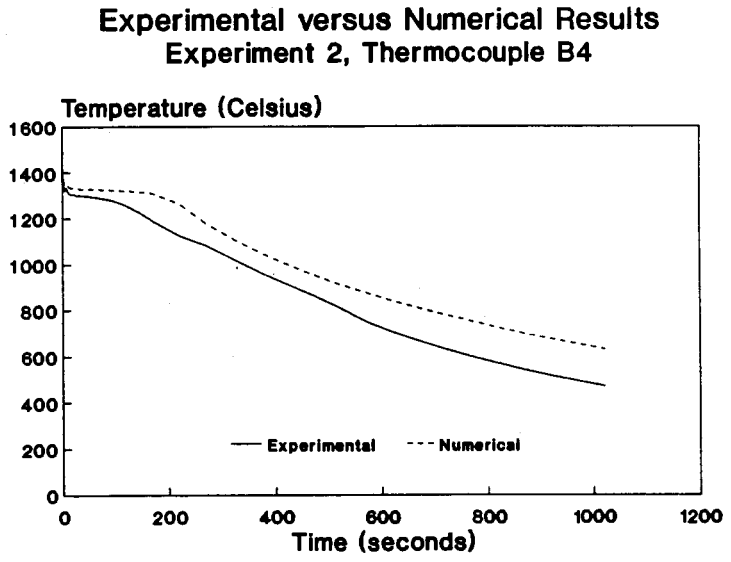

Figure 4.27 Comparison of numerical and experimental temperatures for thermocouple B4.

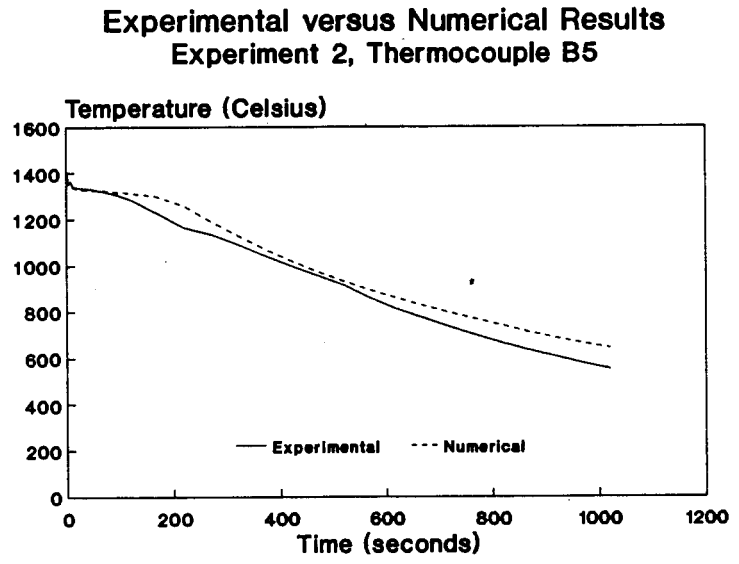

Figure 4.28 Comparison of numerical and experimental temperatures for thermocouple B5.

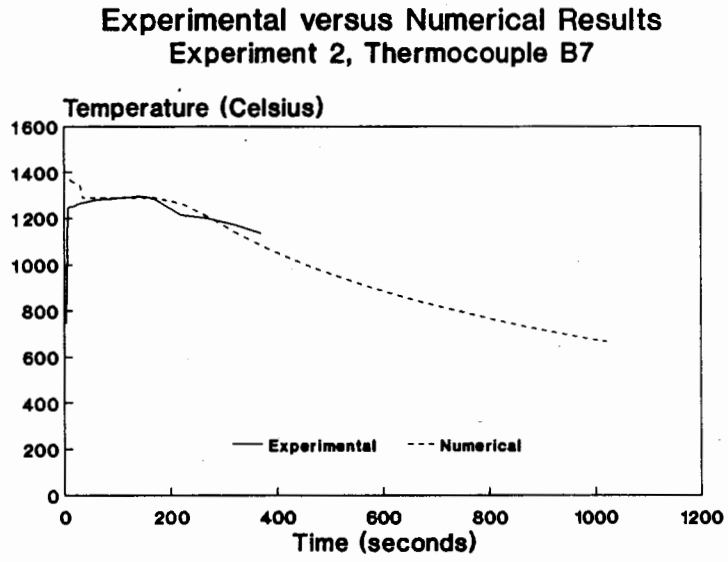

Figure 4.29 Comparison of numerical and experimental temperatures for thermocouple B7.

It is noted in figure 4.20 that thermocouple A4's temperatures are much lower than predicted. This coincides with the observation made in section 4.1.3. The correlation between the numerical and experimental results given above ranges from good to poor. It is noticed that the agreement between numerical and experimental is better during the initial stages of solidification and deteriorates later on. The correlation is also worse for thermocouple positions within the insulation. Possible reasons for the discrepancies are discussed below.

4.2.5 Discussion of Differences

The discrepancies between numerical and experimental temperature histories, given above, can be attributed to uncertainties in the values used for various parameters, experimental error and modelling limitations. It is noticed that the differences are larger during the later stages of comparison. The numerical model is therefore underestimating the heat transfer out of the casting during these latter stages. Poor modelling of boundary conditions and material properties are the most likely cause. Other possible causes are experimental errors and modelling limitations. These are discussed separately below.

4.2.5.1 Uncertainty of Material Properties

Smith et al [26] state that the mould, in this case the ceramic shell and insulation, properties have considerable influence on the solidification rate and need to be accurately modelled to obtain correct solutions. The results of the parametric study, section 4.22, show the significance of the insulation conductivity on the overall results. The conductivity value used in the above analysis was approximated as a constant value, 0.38 W/m $^{\circ}$C, during the one-dimensional study, discussed in section 4.22. The metal and ceramic conductivity and specific heat values are temperature dependent and the use of a constant value for the Koawool is possibly a poor representation of the actual property. The use of realistic temperature dependent conductivity values could improve the correlation between numerical and experimental results.

4.2.5.2 Uncertainty of Boundary Conditions

Errors produced through incorrect convection conditions are considered negligible. The coefficients are calculated using empirical relations and the effect of convection on the overall solution is shown to be small in the parametric study. Errors in modelling boundary conditions are attributed to the uncertainty of exothermic material-metal behaviour, thermal impedance at metal-mould interface and complex radiation behaviour. These are discussed below.

Complex Radiation Conditions

The complex radiation behaviour observed during casting cannot be accurately modelled with the simplistic approach using two constant emissivities determined in the one dimensional study. In the above casting analysis the temperature distribution across the insulation is virtually linear. This is not necessarily correct as the temperature distribution within the absorbing, scattering and emitting insulation will be nonlinear as radiation is a function of the fourth power of temperature. The extent of the nonlinearity depends on the ratio of radiative to conductive heat transfer. Thus the heat transferred from the cooling metal, though the insulation, to the surrounding

environment is poorly modelled. This also explains the poor correlation between numerical and experimental readings for thermocouples within the insulation. This phenomenon needs to be modelled more accurately to improve correlation between numerical and experimental readings. The properties and coefficients required to accurately model this behaviour are not easily measured, and high level of equipment and expertise is required.

Thermal Impedance at Metal-mould Interface

Thermal impedances at the metal-mould interface vary with both time and geometrical position with respect to the casting. The use of a constant value, taken from work performed on a uranium casting and graphite mould, is is probably incorrect. The use of experimentally measured values for the respective surfaces will contribute to improved correlation.

Exothermic Material

In the above casting simulation the consequence of incorrectly modelling the effect of the exothermic material is shown. Although a modelling error may not effect the whole casting, it can lead to incorrect predictions of region likely to experience porosity and void defects. Thus the porosity and void defect prediction and the temperature comparison for thermocouple B7 can be improved by using realistic boundary conditions simulating the exothermic powder effect. This may include heat absorption/generation, convection coefficients and radiation emissivities.

4.2.5.3 Experimental Error

Heisenberg Effect

The temperature within the liquid metal cannot be measured without affecting the value in some way. The thermocouples protective shields act as heat sinks and nucleation sites for solidification. One of the experimental castings was cut through at an interior thermocouple location, by the Division of Materials Science and Technology, to determine the extent of this so called *Heisenberg effect.* The cross section showed a consistent microstructural growth and growth effects induced by the thermocouple were not evident. The thermocouple and measuring equipment are also accurate to within a few degrees and thus it is concluded that the use of thermocouples as measuring devices contributes little towards the discrepancies observed.

Thermocouple Locations

The thermocouple locations within the casting are not accurately known. A scale drawing of the proposed locations was used to estimate where holes needed to be drilled in the ceramic shell mould. The required length of shielding tube and thermocouple was gauged from the drawing, inserted and cemented in position, and thus some positional deviation could easily have occurred. In addition some movement may have taken place due to distortions of the mould and metal. The numerical results presented above use the temperature history of the node closest to the proposed thermocouple site, for comparison with the experimental values. It is thus possible that some discrepancy arises out of incorrect node position. An analysis was performed to determine the sensitivity of the numerical temperature histories to position. Temperature histories of the eight neighbouring nodes are plotted for each of the thermocouple sites to determine the order of magnitude of the possible error. Two such comparisons are shown below in figures 4.23 and 4.24.

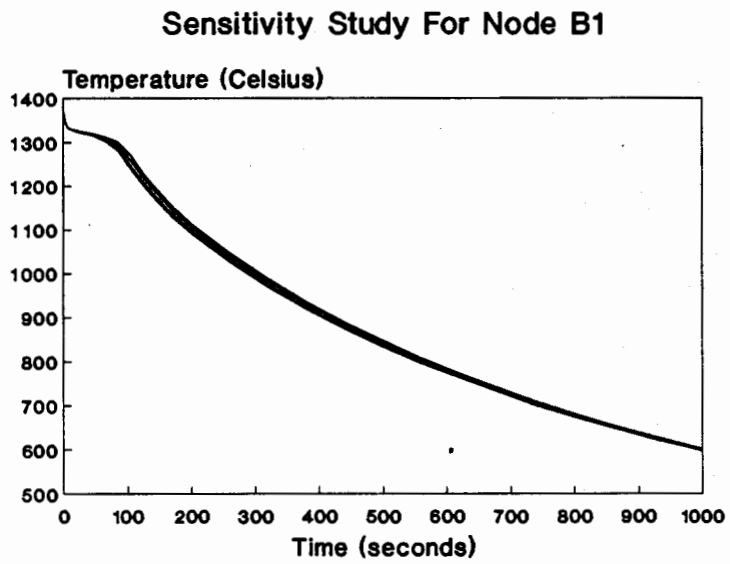

Figure 4.23 Temperature histories for nodes surrounding thermocouple B1.

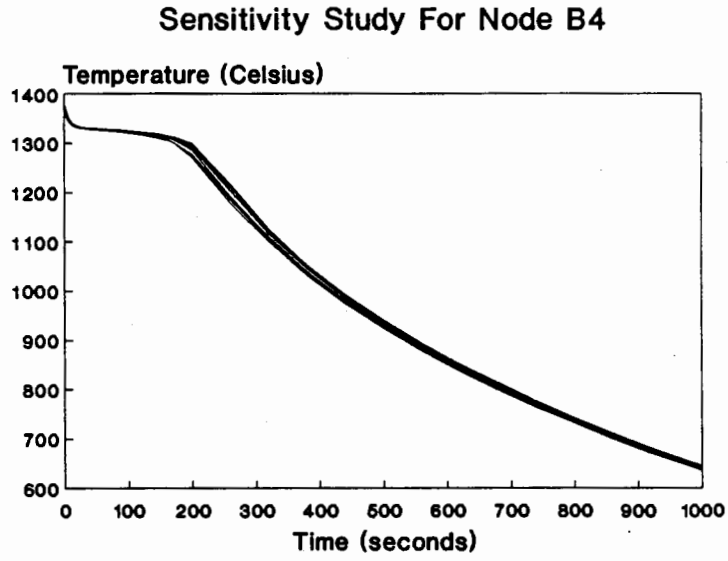

Figure 4.24 Temperature histories for nodes surrounding thermocouple B4.

The maximum distance between any of the eight nodes within each set is less than 1 cm. The maximum temperature difference between surrounding nodes is roughly 50°C. A location error of 1 cm error is possible and could be a contributing factor. This sensitivity analysis highlights the importance of accurately ascertaining the exact thermocouple location.

4.2.5.4 Numerical Model Limitations

Finite Element Mesh

As shown in section 4.2.2, the mesh refinement has a large influence on the solution. The coarse mesh used in the refinement study predicted temperatures which were prolonged at higher values by roughly 1 minute. Similarly the accuracy and correlation could possibly be improved further by increasing the mesh refinement. This will lead to significantly increased computational times.

Excluding Liquid Convection Effects

ABAQUS is not able to model the actual pouring, and thus the initial temperature distribution directly after pour is assumed uniform. This assumption is incorrect and thus the predicted temperatures directly after pour do not agree with measured values. Instantaneous solidification takes place during pouring as the hot metal comes in contact with the cooler mould.

The solidified metal remelts partly as the mould is filled. Thermal gradients are induced during the pouring and the metal and mould temperature fields are not uniform as assumed. Besides influencing microstructure and segregation, convection within the liquid metal also effects the rate of solidification and the shape and size of the mushy zone, and thus alters the temperature distribution within the casting. The increased heat transfer is modelled by increasing the liquid metal conductivity, but the latter effect cannot be artificially simulated. Thus some discrepancy is due to the modelling limitations imposed by the ABAQUS code.

5. Summary and Conclusions

5.1 Summary

The fundamental principles of the foundry process, solidification mechanics and related defects have been presented. An analytical and two numerical methods for solidification modelling have been discussed. The finite element method was found to be the most suitable method for solidification modelling of castings with complex geometries and boundary conditions. A numerical investigation was performed on an investment casting, using the finite element code ABAQUS, to determine its capabilities and limitations.

The casting is an axisymmetric wheel hub, and is cast within a vacuum induction furnace to prevent oxidation of the nickel-based superalloy. Material properties for the metal and alumina silicate shell mould are known, but none are available for the Koawool insulation wrapped around the mould. Values for a glass wool insulation was used and modified to suit. During casting the mould was observed radiating through the fibrous insulation. This constitutes an absorbing, emitting and scattering problem, but is crudely modelled by allowing both outer mould and insulation surfaces to radiate separately to the furnace walls. The thermal impedances at the metal-mould interface are modelled using a constant and conservative gap conductance value. Thermal convection at the insulation-air interface was modelled using coefficients calculated using empirical equations for free convection. Although the convection within the liquid metal is not modelled directly, the additional heat transfer is taken into account by increasing the liquid metal's conductivity tenfold.

A mesh sensitivity study was performed to develop a suitable mesh of the wheel hub casting. A parametric study was performed to determine the influence uncertainties of various parameters had on the solution. The results showed that uncertainties in insulation conductivity and radiation behaviour had large influences on the overall solution. Small variations in gap conductance and convection coefficients had considerably less effect on the solution.

Two experimental castings were conducted to provide measured temperatures for comparison against numerically predicted values. Unfortunately the instrumentation did not record the initial temperatures during the first

experiment. These results were however not discarded, but used in a one dimensional study to approximate the insulation conductivity, and emissivities for mould and insulation surfaces. These estimated values were used in the analysis of the whole casting.

The numerically produced isothermal plots correctly predicted porosity defects in the lower and middle riser region. Analyses performed suggest that these defects can be avoided if the effect of the exothermic material is increased. This could be done by using other exothermic materials releasing more heat, or by containing the evolved heat more successfully by increasing the insulating around and above the upper riser section.

The resultant numerical temperature histories were compared against the experimentally measured values. Two general trends were evident. Firstly, the correlation is best within the casting and deteriorates near the insulation. Secondly, the correlation deteriorates during the latter stages of cooling. It is concluded from these observations and the parametric study mentioned previously, that the major source of numerical differences is the uncertainties in modelling the radiant and conductive heat transfer through the insulation. Other contributing factors are inaccuracies in modelling thermal impedance at metal-mould interface, effect of exothermic material, thermocouple locations and modelling limitations of the ABAQUS code.

5.2 Conclusions

Three numerical techniques were reviewed and the finite element method was found to be the most versatile and suited method for the solidification modelling in complex castings. The general finite element code, ABAQUS, was used to model an investment casting, and correctly predicted regions with porosity and void defects. The correlation of numerically and experimentally determined temperature histories was in general fair (within 10%) during the initial three minutes after pour. The casting has solidified completely by this stage (270 seconds). The solidification is therefore accurately predicted. The predicted cooling subsequent to the solidification is however inaccurate. The major source of differences is ascribed to the uncertainty of material properties and radiation behaviour of the insulation. In spite of these difficulties the numerical model correctly predicted porosity and void defects in the middle and lower riser region. This shows the usefulness of

current modelling techniques in being able to predict defects, and thus reduce the number of prototypes required for process development.

The numerical model developed for this casting example has therefore succeeded in modelling solidification, and qualitatively predicting the porosity and void defects from isotherm plots. The temperatures histories after solidification were however inaccurately predicted. The porosity and void prediction is based on the temperature distribution during solidification and not during the subsequent cooling. Thus the discrepancies observed during the subsequent cooling does not effect the prediction of porosity and void defects. The rate of cooling of the solidified body is however important when attempting to predict the residual stresses and strains, crack formation etc, as these are affected by thermal contractions. The resultant crystal structure e.g. pearlite, martensite, etc does depend on the rate of the subsequent cooling and directly effects the mechanical properties of the casting. However, such complex analyses are beyond the scope of this thesis and thus the current numerical model is considered adequate for the prediction of porosity and void defects. The results obtained are representative for similar casting problems, but are not necessarily representative for the other types, i.e thin section blade castings etc.

5.3 Future Work

The numerical method's accuracy and contribution to the foundry industry can be increased by including other aspects in the numerical model. There is thus scope for further work and improvements in the numerical modelling technique. These aspects are discussed separately.

The material properties and radiation behaviour observed within the insulation needs to be modelled more accurately. Researchers have used various techniques to model the absorbing, emitting and scattering behaviour observed. Tong et al [27] used a *two flux* model and a *linear anisotropic scattering* (LAS) model to calculate the radiative heat transfer within lightweight fibrous insulations, similar to the Koawool used with the investment casting. Glicksman et al [28] used simple transmissivity measurements to predict thermal transfer within foam and fiberglass insulations. Other researchers [29],[30],[31], have used the finite element approach to calculate the heat transfer in absorbing, emitting and scattering media. The formulations and

methods used by these researchers could possibly be included directly in the casting model and the effect on accuracy and correlation determined.

The metal-mould heat transfer coefficient was also identified as a source of discrepancy. Ho et al [4] used a nonlinear estimation technique to solve the inverse heat conduction problem, in order to calculate transient interfacial heat transfer coefficients. Rollett et al [32] used the analytical virtual adjunct method (VAM) to estimate the interfacial heat transfer coefficient. These methods can be used in conjunction with further experimental data to calculate realistic thermal impedances for the various metal-mould contact surfaces. Including these in the current model will improve the accuracy of the predicted heat flow leaving the solidifying metal.

The ability to model fluid flow and convection in the liquid metal is further aspect neglected in the current model. This affects the accuracy with which the the mushy zone and heat flow within the liquid metal are modelled. The pouring cannot be modelled directly and resultant thermal gradients cannot be taken into account without a combined thermo-fluid analysis. Domanus et al [33] used a combined thermal-fluid analysis to model castings. Kubo et al [34] included bulk convection and interdendritic flow to mathematically model shrinkage and gas porosity formation.

Some researchers have developed additional software to manipulate the predicted thermal histories and make predictions about microstructure and defects. Flood et al [35] used a relationship for growth velocity and constitutional undercooling to predict the columnar-equiaxed transition, from numerically calculated thermal histories. Hong et al [36] used three parameters, namely solidification time, temperature gradient and solid fraction gradient, to predict shrinkage cavities. Beffel et al [37] used addition software to predict grain size, hot cracking, shrinkage and were able to use these analyses to select an appropriate alloy for an investment casting of a turbine blade cluster. These techniques could be used to obtain further information from the numerical results already obtained.

A further aspect not included in this thesis is the residual stresses and strains induced during solidification. Thomas et al [38] used a combined thermo-mechanical analysis to investigate cracking within large steel ingots. This type of analysis is able to predict the distortions and residual stresses present within the casting, and can also be used to determine the likelihood

of hot tears and void formation during solidification

The above are examples of technological developments which can be included in the current numerical model, though major software adjustments may be necessary. Including these aspects will contribute to achieving the goals set out for numerical modelling and simulation engineering, i.e to produce improved products with lower associated development costs. A question, however, arises as to the level of modelling required to accurately predict the various defects. This needs to be addressed before large amounts of time and money are spend on developing models including all the aspects outlined above.

REFERENCES

1. Versnyder F L and Shank M E, "The Development of Columnar Grain and Single Crystal High Temperature Materials Through Directional Solidification", Materials Science and Engineering, 6, 213-247, 1970.

2. Taylor P R, "Lost Wax Casting - A Short Illustrated Review", Metallic Materials, 2, 705-710, 1986.

3. Kurz W and Fisher D J, **Fundamentals of Solidification**, Trans Tech Publications, 1986.

4. Flemings M C, **Solidification Processing**, McGraw-Hill Book Company, New York, 1974.

5. Ho K and Pehlke R D, "Metal-Mold Interfacial Heat Transfer", Metallurgical Transactions B, 16B, 585-594, 1985.

6. Planck M, **The Theory of Heat Radiation**, Dover Publications, New York, 1959.

7. Sparrow E M and Cess R D, **Radiation Heat Transfer**, Augmented Edition, McGraw-Hill, 1978.

8. Viskanta R, "Heat Transfer by Conduction and Radiation in Absorbing and Scattering Materials", Journal of Heat Transfer, 87, 143-150, 1965.

9. Campbell J, "Feeding Mechanisms in Castings", Journal for Cast Metals Research, 5, 1-8, 1969.

10. Lecomte-Beckers J, "Study of Microporosity Formation in Nickel-Base Superalloys", Metallurgical Transactions A, 19A, 2341-2348, 1988.

11. Carslaw H S and Jaeger J C, **Conduction of Heat in Solids**, Second Edition, Oxford University Press, London, 1959.

12. Poirer D and Sulcudean M, "On Numerical Methods Used in Mathematical Modelling of Phase Change in Liquid Metals", Journal of Heat Transfer, 110, 562-570, 1988.

13. Sulcudean M and Abdullah Z, "Numerical Simulation of Casting Processes", **Proceedings of VIII International Heat Transfer Conference and Exhibition**, San Fransisco, CA, 1986.

14. Shih T M, **Numerical Heat Transfer**, Hemisphere Publishing Corporation, 1984.

15. Grant G W, "Thermal Modelling of a Permanent Mould Casting Cycle", **Modelling of Casting Welding Process** (edited by Brody H D and Apelian D), 19-37, 1981.

16. Jeanfils C L, Chen J H and Klein H J, "Modelling Solidification in a Electroslag Remelted Ingot", **Modelling of Casting Welding Process** (edited by Brody H D and Apelian D), 313-332, 1981.

17. Lazaridis A, "A Numerical Solution of the Multidimensional Solidification (or Melting) Problem", International Journal of Heat and Mass Transfer, 13, 1459-1476, 1970.

18. Hibbitt, Karlsson and Sorensen, Inc., **ABAQUS Problems Manual**, Version 4.6, Providence, Rhode Island, USA.

19. Lynch D R and O'Neill K. "Continuously Deforming Finite Elements for the Solution of Parabolic Problems, With and Without Phase Change", International Journal of Numerical Methods in Engineering, 17, 81-96, 1981.

20. Belytschko T and Hughes T J R, **Computational Methods for Transient Analysis**, North-Holland, 1983.

21. Vermeer P A and Verruijt A, "An Accuracy condition for Consolidation by Finite Elements", International Journal for Numerical and Analytical Methods in Geomechanics, 5, 1981.

22. Holman J P, **Heat Transfer**, Sixth edition, McGraw-Hill Book Company, 1986.

23. C W Kim and G K Ruthlandt, "3-D Finite Element Method Program for Casting Solidification Simulation", **Modelling and Control of Casting and Welding Processes** (edited by S Kou and R Mehrabian), 557-564, 1986.

24. Harrison C and Weinberg F, "The Influence of Convection on Heat Transfer in Liquid Tin", Metallurgical Transactions B, 16, 355-357, 1985.

25. Rollett A D and Lewis H D, **Finite Element Heat Flow Modelling of Vacuum Induction Casting**, Report LA-UR-85-4469, Materials Science and Technology Division, Los Alamos National Laboratory, 1985.

26. Smith T J, Hoadley A F A and Scott D M, "On the Sensitivity of Numerical Simulations of Solidification to the Physical Properties of the Melt and Mould", Applied Scientific Research, 44, 93-109, 1987.

27. Tong T W, Yang Q S and Tien C L, "Radiative Heat Transfer in Fibrous Insulations - Part 2: Experimental Study", Journal of Heat Transfer, 105, 76-81, 1983.

28. Glicksman L, Schuetz M and Sinofsky M, "Radiation Heat Transfer in Foam Insulation", International Journal of Heat and Mass Transfer, 30, 187-196, 1987.

29. Razżaque M M, Klein D E and Howell J R, "Finite Element Solution of Radiative Heat transfer in a Two-Dimensional Rectangular Enclosure With Gray Participating Media", Journal of Heat Transfer, 105, 933-934, 1983.

30. Razzaque M M, Klein D E and Howell J R, "Coupled Radiative and conductive Heat transfer in a Two-Dimensional Rectangular Enclosure With Gray Participating Media using Finite Elements", Journal of Heat Transfer, 106, 613-619, 1984.

31. Chung T J and Kim J Y, "Two-Dimensional Combined-Mode Heat Transfer by Conduction, Convection and Radiation in Emitting, Absorbing and Scattering Media - Solution by Finite Elements", Journal of Heat Transfer, 106, 448-452, 1984.

32. Rollett A D, Lewis H D and Dunn P S, "Measurement and Modelling of Interface Heat Transfer Coefficients", **Modelling and Control of Casting and Welding Processes** (edited by S Kou and R Mehrabian), 565-575, 1986.

33. Domanus H M, Liu Y Y and Sha W T, "Fluid Flow and Heat Transfer Modelling for Castings", **Computer Simulation of Microstructural Evolution** (edited by Srolovitz D J), 361-375.

34. Kubo K and Pehlke R D, "Mathematical Modelling of Porosity Formation in Solidification", Metallurgical Transactions B, 16B, 359-366, 1985.

35. Flood S C and Hunt J D, "Numerical Study of Columnar -Equiaxed Transition", **Modelling of Casting and Welding Processes II** (edited by Dantzig J A and Berry J T), 207-218, 1984.

36. Hong C P, Umeda T and Kimura Y, "Applications of the Boundary Method to Solidification Problems", **Modelling of Casting and Welding Processes II** (edited by Dantzig J A and Berry J T), 221-236, 1984.

37. Beffel M J, Yu K O, Robinson M and Schneider K R, "Computer Simulation of Investment Casting Process", Journal of Metals, 27-30, February 1989.

38. Thomas B G, Samarasekera I V and Brimacombe J K, "Applications of Mathematical Heat Flow and Stress Models of Steel Ingot Casting to Investigate Panel Crack Formation", **Modelling and Control of Casting and Welding Processes** (edited by Kou S and Mehrabian R), 479-495, 1986.

APPENDIX A

FINITE ELEMENT ACCURACY CONDITION FOR HEAT TRANSFER

The accuracy condition formulated below is for a simple 1-dimensional transient heat transfer problem with fixed temperature boundary conditions. The radiation and convection boundary conditions are neglected for this analysis. The problem domain is of length 2ℓ. The governing equation is given by equation (2.3), and is given by,

$$K\frac{\partial^2 T}{\partial x^2} + Q = \rho C \frac{\partial T}{\partial t} \qquad (A.1)$$

for the 1-dimensional case. The initial temperatures are defined by,

$$T(t=0) = T^{\circ}$$

with the temperature on the boundary defined by a fixed value,

$$T(t) = T$$

where K, ρ and C are the conductivity, density and specific heat respectively
Q is the heat generation term.

The resultant finite element equation is given in equation (3.17),

$$[M]\dot{T} + [K]T - F = 0 \qquad (A.2)$$

where

$$M_{ij} = \sum_{n=1}^{E} \int_x \rho\, C\, N_i N_j \frac{\partial T}{\partial T}\, dx$$

$$K_{ij} = \sum_{n=1}^{E} \int_x K \frac{dN_i}{dx} \frac{dN_j}{dx}\, dx$$

$$F_j = \sum_{n=1}^{E} \int_x Q\, N_j\, dx$$

The differential equation (A.2) is integrated with respect to time using the general trapezoidal rule. The value of φ defines the particular trapezoidal method being used, e.g. the integral of function ϕ is

$$\int_{t^0}^{t^1} \phi \, dt = \left((1-\varphi)\phi^0 + \varphi\phi^1\right)\Delta t = (\phi^0 + \varphi\,\Delta\phi)\Delta t \qquad \text{(A.3)}$$

where superscripts 0 and 1 denote the values at the beginning and end of the time step. The increments Δt and $\Delta\phi$ are defined by,

$$\Delta t = t^1 - t^0 \qquad \Delta\phi = \phi^1 - \phi^0 \qquad \text{(A.4)}$$

Using these scheme to integrate equation (A.2) over the time interval $t = t^0$ to $t = t^1$ gives,

$$[M]\Delta T + [K](T^0 - \varphi\,\Delta T)\Delta t - \Delta F = 0 \qquad \text{(A.5)}$$

where $\Delta T = T^1 - T^0$

$\Delta t = t^1 - t^0$

with **T** constant and $\Delta T = 0$ at the boundaries $x = 0$ and $x = 2h$. Equation (A.5) can be rewritten as

$$\frac{1}{\ell}\left([M] + \varphi\Delta t[K]\right)\Delta T = \frac{\Delta F}{\ell} - [K]T^0 \qquad \text{(A.6)}$$

The accuracy condition is shown for a 1-dimensional isoparametric element. The element layout is shown below.

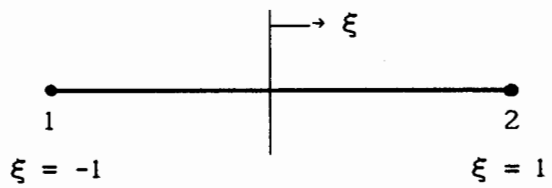

where ξ is the normal coordinate of the element and is related to the global **x** coordinate by,

$$\xi = \frac{2x - (x_e + x_{e+1})}{\ell}$$

The two shape functions are given by,

$$N_1 = \frac{1}{2}(1 - \xi) \qquad N_2 = \frac{1}{2}(1 + \xi)$$

The Jacobian J for these shape functions is,

$$J = \frac{\partial x}{\partial \xi} = \frac{\ell}{2}$$

The integrals **M**, **K** and **F** can be evaluated in terms of these shape functions and the Jacobian.

$$M_{ij} = \int_{Xe}^{Xe+1} \rho\, C\, N_i\, N_j\, dx = \int_{-1}^{1} \rho\, C\, N_i\, N_j \frac{dx}{d\xi}\, d\xi$$

$$K_{ij} = \int_{Xe}^{Xe+1} K \frac{dN_i}{dx}\frac{dN_j}{dx}\, dx = \int_{-1}^{1} K \frac{dN_i}{d\xi}\frac{dN_j}{d\xi}\frac{d\xi}{dx}\frac{d\xi}{dx}\frac{dx}{d\xi}\, d\xi = \int_{-1}^{1} K \frac{dN_i}{d\xi}\frac{dN_j}{d\xi}\frac{d\xi}{dx}\, d\xi$$

$$F_j = \int_{Xe}^{Xe+1} Q\, N_i\, dx = \int_{-1}^{1} Q\, N_i \frac{dx}{d\xi}\, d\xi$$

Evaluating these for the 1-dimensional linear element described gives,

$$\mathbf{M} = \frac{\rho C \ell}{6}\begin{bmatrix} 2 & 1 \\ 1 & 2 \end{bmatrix} \qquad \mathbf{S} = \frac{K}{\ell}\begin{bmatrix} 1 & -1 \\ -1 & 1 \end{bmatrix} \qquad \mathbf{F} = \frac{Q\ell}{2}\begin{bmatrix} 1 \\ 1 \end{bmatrix}$$

Substituting theses matrices into equation (A.6) and neglecting boundary temperature change terms (ΔT_1 and ΔT_n, as both are zero) gives,

$$\begin{bmatrix} 1-2b & b & & & \\ & 1-2b & b & & \\ & \cdots & \cdots & \cdots & \\ & & b & 1-2b & b \\ & & & b & 1-2b \end{bmatrix}\begin{bmatrix} \Delta T_2 \\ \Delta T_3 \\ \cdots \\ \Delta T_{n-2} \\ \Delta T_{n-1} \end{bmatrix} = \Delta Q \begin{bmatrix} 1 \\ 1 \\ \cdots \\ 1 \\ 1 \end{bmatrix} - \frac{K\Delta t}{\ell^2}\begin{bmatrix} -1 & 2 & -1 & & \\ & -1 & 2 & -1 & \\ & & \cdots & \cdots & \cdots \\ & & & -1 & 2 & -1 \\ & & & & -1 & 2 & -1 \end{bmatrix}\begin{bmatrix} T_1^o \\ T_2^o \\ \cdots \\ T_{n-2}^o \\ T_{n-1}^o \\ T_n^o \end{bmatrix} \qquad \text{(A.7)}$$

where

$$b = \frac{\rho C}{6} - \varphi \frac{K(\Delta t)}{\ell^2} \qquad \text{(A.8)}$$

The solution of ΔT can be divided into two parts, each corresponding to one of the terms on the right-hand side. The first part of the solution is determined by the heat generation load ΔQ, and will be denoted by $\Delta T'$. The first part of the

solution is can be written as,

$$\begin{bmatrix} 1-2b & b & & & \\ & 1-2b & b & & \\ & \cdot\cdot & \cdots & \cdot\cdot & \\ & & b & 1-2b & b \\ & & & b & 1-2b \end{bmatrix} \begin{bmatrix} \Delta T'_2 \\ \Delta T'_3 \\ \cdots \\ \Delta T'_n \\ \Delta T_{n-1} \end{bmatrix} = \Delta Q \begin{bmatrix} 1 \\ 1 \\ \cdots \\ 1 \\ 1 \end{bmatrix} \qquad \text{(A.9)}$$

A limit is placed on the maximum value of $\Delta T'$, to prevent the solution oscillating due to the internal load Q. The value of the numerically predicted $\Delta T'$ must be smaller or at most equal to the exact temperature change $\Delta \hat{T}$. Thus the numerical model must not exaggerate the temperature change caused by the internal heat generation load. This can also be stated as,

$$\Delta T' \leq \Delta Q \qquad \text{(A.10)}$$

This may also be expressed in terms of e_i as follows,

$$\Delta T'_i = \Delta Q \ (1 - e_i)$$

and the criterion (A.10) becomes

$$e_i \geq 0 \qquad (i = 2, 3, \ldots, n-1) \qquad \text{(A.11)}$$

Substituting (A.11) into (A.9) and neglecting boundary terms gives,

$$\mathbf{e} - b\mathbf{S}^*\mathbf{e} = -b\mathbf{g} \qquad \text{(A.12)}$$

where **e**, $\mathbf{S}^*$ and **q** are defined as follows

$$\mathbf{e} = \begin{bmatrix} e_2 \\ e_3 \\ e_4 \\ \cdots \\ e_{n-2} \\ e_{n-1} \end{bmatrix}, \quad \mathbf{S}^* = \begin{bmatrix} 2 & -1 & & & & & \\ -1 & 2 & -1 & & & \cdot & \\ & -1 & 2 & -1 & & & \\ & & \cdot\cdot & \cdot\cdot & \cdot\cdot & & \\ & & & & -1 & 2 & -1 \\ & & & & & -1 & 2 \end{bmatrix}, \quad \mathbf{g} = \begin{bmatrix} 1 \\ 0 \\ 0 \\ \cdots \\ 0 \\ 1 \end{bmatrix} \qquad \text{(A.12)}$$

Multiplying equation (A.12) through by $\mathbf{e}^T$ gives a scalar equation,

$$\mathbf{e}^T(\mathbf{I} - b\mathbf{S}^*)\mathbf{e} = -b(e_2 + e_{n-1}) \qquad \text{(A.13)}$$

where **I** is the identity matrix. From equation (A.8) it can be seen that b is

always smaller than $\frac{1}{6}$ and hence the left-hand side of (A.12) is always positive. The right-hand side must therefore also be positive. This can be expressed as,

$$- b(e_2 + e_{n-1}) \geq 0$$

Thus for a solution which converges incrementally in monotonic fashion, i.e.

$$e_i \geq 0$$

the parameter b has to be negative or zero, i.e.

$$b \leq 0$$

This implies a minimum bound on the time step, which can be obtained directly from equation (A.8).

$$\frac{\rho\ C}{6} - \varphi \frac{K(\Delta t)}{\ell^2} \leq 0$$

This gives,

$$\Delta t \geq \frac{\rho\ C\ \ell^2}{6\ \varphi\ K} \qquad \text{(A.15)}$$

This defines the lower limit for the time step Δt in terms of material properties and element length, which will prevent solution oscillation due to the applied heat generation load. This internal heat generation load can also be used to model the latent heat liberated during phase change, i.e.

$$Q = \rho\ L \frac{df_L}{dt}$$

where L is the latent heat liberated per unit mass,
and f_s is the solid fraction within the material.

Thus it is important to consider the time step used when modelling heat generation or phase changes. Equation (A.15) is identical to equation (4.1) for the difference scheme (φ=1).

APPENDIX B

CALCULATION OF CONVECTION COEFFICIENTS

The convection coefficients for the various surfaces are calculated using empirical relations for free convection from isothermal horizontal and vertical flat plates. Coefficients for each surface are calculated at the estimated highest and lowest surface temperature and the transient convection coefficient is assumed to be remain within these limits. The formulas used are shown below with one worked example. The other calculated coefficients are calculated in the same manner and merely listed.

$$\bar{h}_c = \overline{Nu}_f \frac{K}{l} \tag{B.1}$$

$$\overline{Nu}_f = D\,(Ra_f)^m \tag{B.2}$$

$$Ra_f = Gr_f\, Pr_f \tag{B.3}$$

$$Pr_f = \frac{\nu}{\alpha} \tag{B.4}$$

$$Gr_f = \frac{g_r l \beta^3 \Delta T}{\nu^2} \tag{B.5}$$

Where $\bar{h}_c$ is the average convection coefficient for the surface at a particular temperature,

$\overline{Nu}$ is the Nusselt number,

Ra is the Rayleigh number,

Pr is the Prandtl number,

Gr is the Grashof number,

K is the fluids conductivity,

ν is the fluids kinematic viscosity

α is the thermal diffusivity of the fluid

β is the fluids volumetric coefficient of expansion, and for air is given by the inverse of its absolute temperature.

g_r is the acceleration due to gravity,

l is the surface dimension,

ΔT is the difference between the surface and ambient temperatures,

subscript f indicates that the properties in the dimensionless groups are evaluated at the film temperature T_f, which is defined as the average of the surface temperature T_w and ambient fluid temperature T_∞.

D and m are constants dependent on surface geometry and Rayleigh number.

The values used for the constants D and m are given below. **1.** For vertical plates,

$$D = 0.59 \quad \text{and} \quad m = \frac{1}{4} \qquad \text{for} \quad 10^4 \leq Ra_f \leq 10^9$$

2. For horizontal plates with the upper surface heated,

$$D = 0.54 \quad \text{and} \quad m = \frac{1}{4} \qquad \text{for} \quad 2\times10^4 \leq Ra_f \leq 8\times10^6$$

3. For horizontal plates with the lower surface heated,

$$D = 0.27 \quad \text{and} \quad m = \frac{1}{4} \qquad \text{for} \quad 10^5 \leq Ra_f \leq 10^{11}$$

The respective surfaces for which the coefficients are calculated are shown below in figure B.1

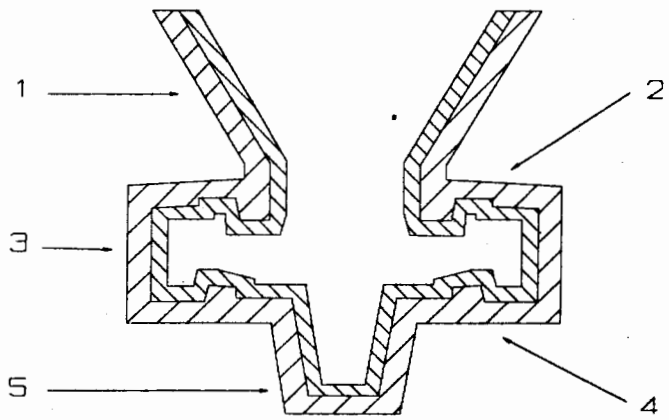

Figure B.1 Surfaces for which convection coefficients are calculated.

The coefficient used for the surfaces 1, 3 and 5 is calculated using the average surface dimension, 8 cm. The coefficients for surfaces 2 and 4 are calculated separately.

Example Calculation for Combined Surfaces 1,3 & 5

This coefficient is calculated using the average surface dimension. Coefficients are calculated for surface temperatures of 500°C and 160°C respectively with a constant ambient temperature of 30°C.

1. Calculated convection coefficient at 500°C with ambient air at 30°C.

$$l = 0.08 \text{ m}$$

$$T_f = \frac{1}{2}(500 + 30) = 265^\circ C$$

The following properties for air at 265°C are interpolated for from tables.

$$K = 0.04283 \text{ W/m } ^\circ C$$

$$\nu = 42.794 \times 10^{-6} \text{ m}^2/\text{s}$$

$$\alpha = 0.6300 \text{ m}^2/\text{s}$$

$$Pr = 0.68$$

$$\beta = 1.8587 \times 10^{-3}$$

The calculation proceeds as follows,

$$Gr_f = \frac{9.81 \times 1.8587 \times 10^{-3} \times (500-30) \times 0.08^3}{(42.794 \times 10^{-6})^2} = 2.396 \times 10^6$$

$$Ra_f = 2.396 \times 10^6 \times 0.68 = 1.629 \times 10^6$$

$$\overline{Nu}_f = 0.59 \times \left(1.629 \times 10^6\right)^{1/4} = 21.08$$

$$\bar{h}_c = 21.08 \times \frac{0.04283}{0.08} = 11.28 \text{ W/m}^2 \,^\circ C$$

2. Calculated convection coefficient at 160°C with ambient air at 30°C.

$$T_f = \frac{1}{2}(160 + 30) = 95^\circ C$$

The following properties for air at 265°C are interpolated for from tables.

$$K = 0.03133 \text{ W/m } ^\circ\text{C}$$

$$\nu = 22.610 \times 10^{-6} \text{ m}^2/\text{s}$$

$$\alpha = 0.3263 \text{ m}^2/\text{s}$$

$$Pr = 0.694$$

$$\beta = 2.7174 \times 10^{-3}$$

The calculation proceeds as follows,

$$Gr_f = \frac{9.81 \times 2.7174 \times 10^{-3} \times (160-30) \times 0.08^3}{(22.610 \times 10^{-6})^2} = 3.471 \times 10^6$$

$$Ra_f = 3.471 \times 10^6 \times 0.68 = 2.360 \times 10^6$$

$$\overline{Nu}_f = 0.59 \times \left(2.360 \times 10^6\right)^{1/4} = 23.12$$

$$\bar{h}_c = 23.12 \times \frac{0.03133}{0.08} = 9.06 \text{ W/m}^2 \text{ }^\circ\text{C}$$

The transient coefficient for surfaces 1, 3 and 5 are therefore assumed to vary between 11.28 and 9.06 W/m^2 °C.

The coefficients calculated for surfaces 2 and 4 are given below:

Surface 2	at 500°C	$\bar{h}_c = 10.67$ W/m^2 °C
	at 160°C	$\bar{h}_c = 8.61$ W/m^2 °C
Surface 4	at 500°	$\bar{h}_c = 5.25$ W/m^2 °C
	at 160°C	$\bar{h}_c = 4.23$ W/m^2 °C

APPENDIX C

MATERIAL PROPERTIES FOR THE METAL AND CERAMIC MOULD

The material properties for the nickel-based superalloy and alumina silicate mould material are given as temperature dependent values. These are tabulated below for the two materials.

Nickel-based superalloy, Inconel 713LC

Liquidus temperature = 1330°C
Solidus temperature = 1290°C
Latent heat of fusion = 141.750 KW/Kg

Temperature °C	Conductivity W/m°C	Specific Heat J/Kg°C	Density Kg/m^3
21	9.0	440.	8000.
93	10.7	460.	"
205	12.1	500.	"
315	13.7	525.	"
425	15.3	545.	"
540	16.7	565.	"
650	18.3	585.	"
760	20.0	625.	"
870	21.7	670.	"
980	23.1	690.	"
1090	25.3	710.	"

Table C 1 Material properties for the nickel-based superalloy, Inconel 713LC

Alumina silicate ceramic mould

Temperature °C	Conductivity W/m°C	Specific Heat J/Kg°C	Density Kg/m
0	188.0	1101.	2100.
20	188.3	1120.	"
100	188.3	1165.	"
200	186.2	1203.	"
300	184.1	1254.	"
400	180.5	1298.	"
500	175.0	1351.	"
600	168.2	1419.	"
601	90.0	1343.	"
700	95.5	1312.	"
800	98.2	1260.	"

Table C 2 Material properties for the alumina silicate mould.

Appendix D

Isotherms During Solidification

The following figures show the progression of the solidification front through the casting. The time after pour is indicated beneath each figure.

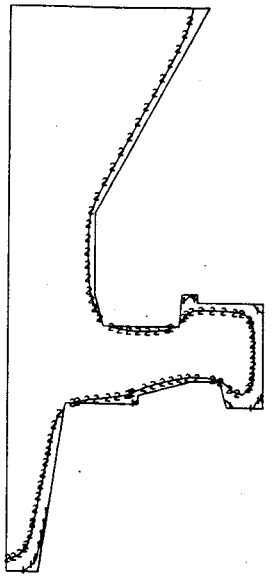

3 seconds after pour.

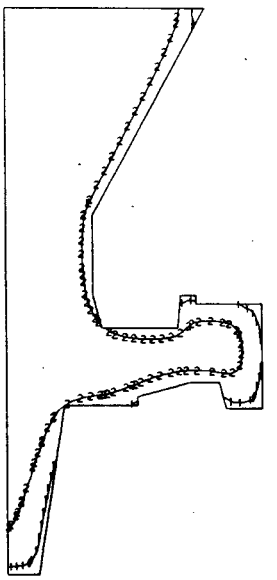

7 seconds after pour.

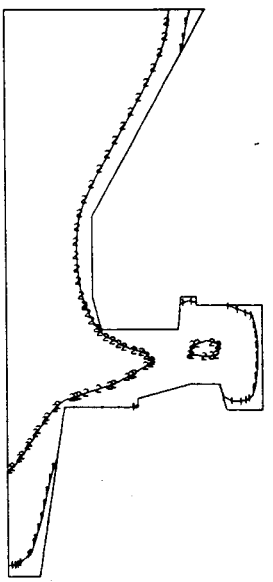

12 seconds after pour.

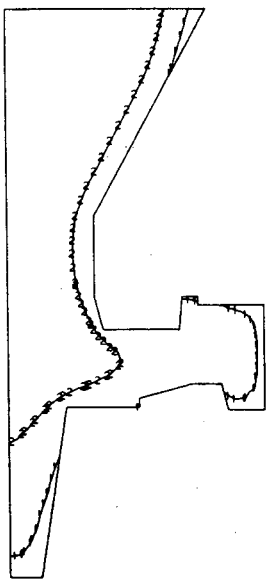

17 seconds after pour.

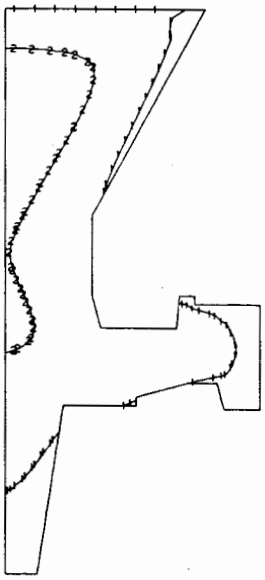

45 seconds after pour.

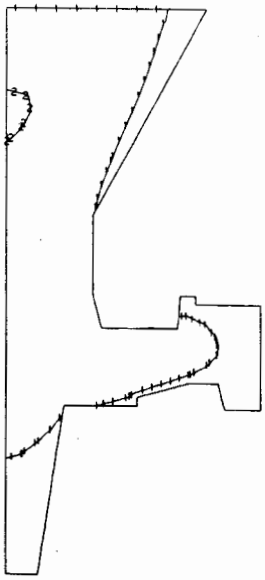

65 seconds after pour.

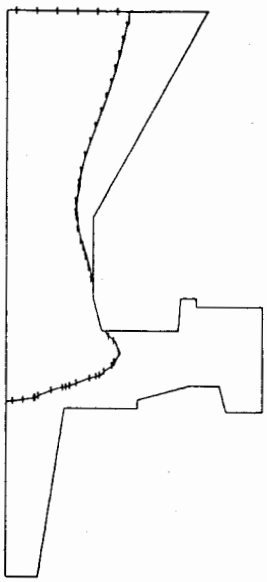

135 seconds after pour.

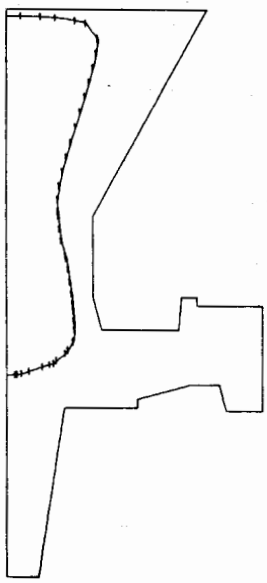

180 seconds after pour.

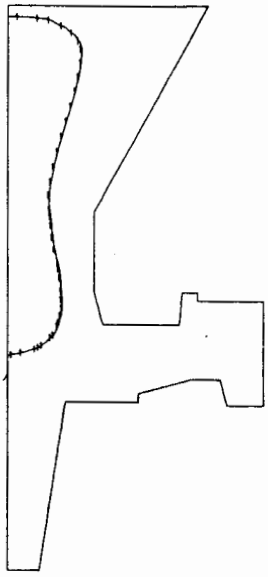

200 seconds after pour.

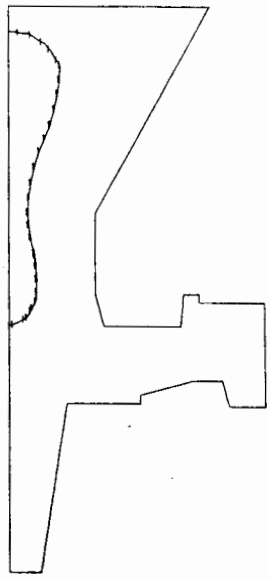

230 seconds after pour.

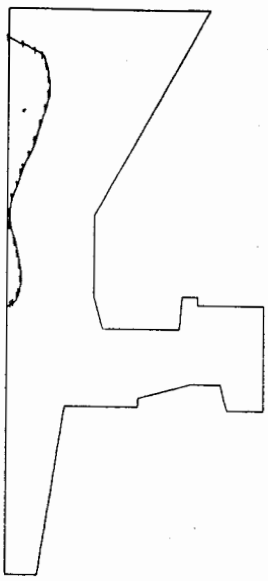

240 seconds after pour.

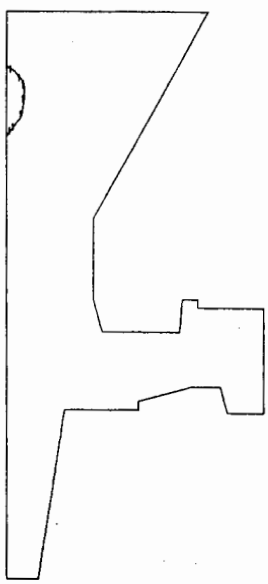

260 seconds after pour.

APPENDIX E

Courses completed in partial fulfillment of the M.Sc. Degree

Course		Date	Credits
CIV 540F	Finite Element Analysis	1988	4
CIV 588F	Applied Mechanics I	1988	3
CIV 588F	Applied Mechanics II	1988	3
CIV 593S	Engineering Software Design and Development	1988	3
AMA 363F	Numerical Analysis	1988	3
AMA 367F	Continuum Mechanics	1988	3
AMA 368S	Numerical Solution of Differential Equations	1988	3
		TOTAL	22

Course Credits : 22

Thesis Credits : 20

TOTAL 42

Minimum credit requirements for the M.Sc. (Eng) Degree : 40

CIV 540 Finite Element Analysis

Generalised displacement method of analysis. Elastic energy theorems leading to basic procedures of the finite element method. Approximation and interpolation of functions. Isoparametric formulation of elements. 2-D and 3-D elements of structural mechanics. Equation solving in the computer and the structure of the finite element program. Introduction to finite element packages for practical applications. Some advanced topics in finite element analysis.

CIV 588F Applied Mechanics I

Concepts of stress, strain, compatibility. Equilibrium equations and constitutive relationships. Applications to beams, rods, plates and two dimensional elasticity. Solutions of simple boundary value problems in plane stress/strain and plates. Energy concepts in mechanics.

CIV 589S Applied Mechanics II

Variational calculus and variational principles in mechanics; virtual work, minimum potential energy, Reissner. Methods of approximation leading to the finite element method applied to plates and shells. Potential problems. Topics in nonlinear mechanics-plasticity, geometric nonlinearity, creep.

CIV 593S Engineering Software Design and Development

Microcomputer hardware components, DOS operating system, software design methodologies, modularity and information hiding, logic and decision tables, data abstraction and file handling. Testing and debugging. Man-machine interface and computer graphics. Software tools and packages. Numerical representation and accuracy.

AMA 363F Numerical Analysis

Introduction to some topics in numerical analysis, with applications to modelling. Numerical methods of solution to ordinary differential equations; approximations to functions; eigenvalue methods. Modelling examples.

AMA 367F Continuum Mechanics

Introduction to tensors with applications to fluid mechanics and elasticity. Tensor algebra and analysis, fluid and solid mechanics, Navier-Stokes equations, the partial differential equations of elasticity, examples.

AMA 368S Numerical Solution of Differential Equations

Introduction to commonly used methods for solving partial differential equations numerically. Introduction to the finite element method for partial differential equations, analysis of the finite element method, finite difference methods.